DRAFT
CMS Paper

The content of this note is intended for CMS internal use and distribution only

A search for new phenomena in pp collisions at $\sqrt{s} = 13\,\text{TeV}$ in final states with missing transverse momentum and at least one jet using the α_T variable

The CMS Collaboration

Abstract

A search for new phenomena is performed in final states containing one or more jets and an imbalance in transverse momentum in pp collisions at a centre-of-mass energy of 13 TeV. The analysed data sample, recorded with the CMS detector at the CERN LHC, corresponds to an integrated luminosity of $2.3\,\text{fb}^{-1}$. Several kinematic variables are employed to suppress the dominant background, multijet production, as well as to discriminate between other standard model and new physics processes. The search provides sensitivity to a broad range of new-physics models that yield a stable weakly interacting massive particle. The number of observed candidate events is found to agree with the expected contributions from standard model processes, and the result is interpreted in the mass parameter space of fourteen simplified supersymmetric models that assume the pair production of gluinos or squarks and a range of decay modes. For models that assume gluino pair production, masses up to 1575 and 975 GeV are excluded for gluinos and neutralinos, respectively. For models involving the pair production of top squarks and compressed mass spectra, top squark masses up to 400 GeV are excluded.

DRAFT

1 Introduction

The standard model (SM) of particle physics is successful in describing a wide range of phenomena, although it is widely believed to be only an effective approximation of a more complete theory that supersedes it at a higher energy scale. Supersymmetry (SUSY) [1–4] is a modification to the SM that extends its underlying space-time symmetry group. For each boson (fermion) in the SM, a fermionic (bosonic) superpartner, which differs in spin by one-half unit, is introduced.

Experimentally, SUSY is testable through the prediction of an extensive array of new observable states (of unknown masses) [5, 6]. In the minimal supersymmetric extension to the SM [6], the gluinos $\widetilde{g}$, light- and heavy-flavour squarks $\widetilde{q}, \widetilde{b}, \widetilde{t}$, and sleptons $\widetilde{\ell}$ are, respectively, the superpartners to gluons, quarks, and leptons. An extended Higgs sector is also predicted, as well as four neutralino $\widetilde{\chi}^0_{1,2,3,4}$ and two chargino $\widetilde{\chi}^\pm_{1,2}$ states that arise from mixing between the higgsino and gaugino states, which are the superpartners of the Higgs and electroweak gauge bosons. The assumption of R-parity conservation [7] has important consequences for cosmology and collider phenomenology. Supersymmetric particles are expected to be produced in pairs at the LHC, with heavy states decaying eventually to the stable lightest SUSY particle (LSP). The LSP is generally assumed to be the $\widetilde{\chi}^0_1$, which is weakly interacting and massive. This SUSY particle is considered to be a candidate for dark matter (DM) [8], the existence of which is supported by astrophysical data [9]. Hence, the characteristic signature of natural SUSY production at the LHC is a final state containing an abundance of jets, possibly originating from top or bottom quarks, accompanied by a significant transverse momentum imbalance, $\vec{p}_T^{\text{miss}}$.

The proposed supersymmetric extension of the SM is also compelling from a theoretical perspective, as the addition of superpartners to SM particles can modify the running of the gauge coupling constants such that their unification can be achieved at a high energy scale [10–12]. A more topical perspective, given the recently discovered Higgs boson [13–15], is the possibility that the superpartners can alleviate the gauge hierarchy problem of the SM by compensating for radiative corrections to the Higgs boson mass from loop processes involving SM particles [16, 17]. These corrections have a power-law dependence on scale, which can only be accommodated in the SM through an extreme level of fine tuning of the bare Higgs boson mass. A "natural" solution from SUSY, with minimal fine-tuning, implies that the masses of the gluino, the third-generation squarks, and a (higgsino-like) $\widetilde{\chi}^0_1$ are at or near the electroweak scale [18].

The lack of evidence to date for SUSY has also focused attention on regions of the parameter space with sparse coverage, which include natural models [19–23]. For example, models in which both the $\widetilde{t}$ and the $\widetilde{\chi}^0_1$ are light and nearly degenerate in mass are phenomenologically well motivated [24–27]. This class of models, with "compressed" mass spectra, typically yield SM particles with low transverse momenta (p_T) from the decays of SUSY particles. Hence, searches rely on the associated production of jets, often resulting from initial-state radiation (ISR), to achieve experimental acceptance.

This paper presents an inclusive search for new-physics phenomena in hadronic final states with one or more energetic jets and an imbalance in $\vec{p}_T^{\text{miss}}$, performed in proton-proton (pp) collisions at a centre-of-mass energy $\sqrt{s} = 13\,\text{TeV}$. The analysed data sample corresponds to an integrated luminosity of $2.3 \pm 0.1\,\text{fb}^{-1}$ collected by the CMS experiment. Earlier searches using the same technique have been performed in pp collisions at both $\sqrt{s} = 7$ [28–30] and 8 TeV [31, 32] by the CMS Collaboration. The increase in the centre-of-mass energy of the LHC, from $\sqrt{s} = 8$ to 13 TeV, provides a unique opportunity to search for the characteristic signatures of new physics at the TeV scale. For example, the increase in $\sqrt{s}$ leads to a factor $\gtrsim 35$ increase

48 in the parton luminosity [33] for the pair production of coloured SUSY particles, each of mass
49 1.5 TeV, which were beyond the reach of searches performed at $\sqrt{s} = 8$ TeV by the ATLAS [34,
50 35] (and references therein) and CMS [36–43] Collaborations. Several searches in this final state,
51 interpreted within the context of SUSY, have already provided results with the first data at this
52 new energy frontier [44–50].

53 An inclusive strategy is adopted to ensure sensitivity to the broadest possible region of the
54 SUSY parameter space. The strategy focuses on maintaining high acceptance through the ap-
55 plication of selection criteria with the lowest possible thresholds, and the categorisation of can-
56 didate signal events according to multiple discriminating variables. The search is sufficiently
57 generic and inclusive to provide sensitivity to a wide range of non-SUSY models that postulate
58 the existence of a stable, weakly interacting, massive particle. In addition to the jets $+ \vec{p}_{\mathrm{T}}^{\mathrm{miss}}$
59 topology, the search considers final states containing a "monojet" topology, which is expected
60 to improve the sensitivity to DM particle production in pp collisions [51, 52].

61 This search is based on an examination of the number of reconstructed jets per event, the
62 number of these jets identified as originating from bottom quarks, and the scalar and vector
63 p_{T} sums of these jets. These variables provide sensitivity to the different production mecha-
64 nisms (squark-squark, squark-gluino, and gluino-gluino) of massive coloured SUSY particles
65 at hadron colliders, third-generation squark signatures, and both large and small mass split-
66 tings between the parent SUSY particle and the LSP.

67 The dominant background process for a search in all-jet final states is multijet production, a
68 manifestation of quantum chromodynamics (QCD). An accurate estimate of this background
69 is difficult to achieve, given the lack of precise theoretical predictions for the multijet produc-
70 tion cross section and kinematic properties. Hence, this search adopts a strategy that employs
71 several variables to reduce the multijet contribution to a low level with respect to other SM
72 backgrounds, rather than estimate a significant contribution with high precision.

73 The search is built around two variables that are designed to provide robust discrimination
74 against multijet events at the energy and luminosity frontier. A dimensionless kinematic vari-
75 able α_{T} [28, 53] is constructed from jet-based quantities and provides discrimination between
76 genuine sources of $\vec{p}_{\mathrm{T}}^{\mathrm{miss}}$ from stable, weakly interacting particles such as neutrinos or neu-
77 tralinos that escape the detector, and instrumental sources such as the mismeasurements of jet
78 energies. The $\Delta\phi_{\mathrm{min}}^{*}$ [28] variable exploits azimuthal angular information and also provides
79 strong rejection power against multijet events, including rare energetic events in which neu-
80 trinos carry a significant fraction of the energy of a jet due to semileptonic decays of heavy-
81 flavour mesons. Very restrictive requirements on the α_{T} and $\Delta\phi_{\mathrm{min}}^{*}$ variables are employed in
82 this search to ensure a low level of contamination from the multijet background.

83 The organisation of this paper is as follows. Sections 2 and 3 describe, respectively, the CMS
84 apparatus and the simulated event samples. Sections 4 and 5 describe the event reconstruction
85 and selection criteria used to identify candidate signal events and control region samples. Sec-
86 tion 6 provides details on the estimation of the multijet and all other SM backgrounds. Finally,
87 the search results and interpretations, in terms of simplified SUSY models, are described in
88 Sections 7 and 8, and summarised in Section 9.

89 2   The CMS detector

90 The central feature of the CMS apparatus is a superconducting solenoid of 6 m internal diam-
91 eter, providing an axial magnetic field of 3.8 T. The bore of the solenoid is instrumented with

several particle detection systems. A silicon pixel and strip tracker measures charged particles within the pseudorapidity range $|\eta| < 2.5$. A lead tungstate crystal electromagnetic calorimeter (ECAL), and a brass and scintillator hadron calorimeter (HCAL), each composed of a barrel and two endcap sections, extend over a range $|\eta| < 3.0$. Outside the bore of the solenoid, forward calorimeters extend the coverage to $|\eta| < 5.0$, and muons are measured within $|\eta| < 2.4$ by gas-ionisation detectors embedded in the steel flux-return yoke outside the solenoid. A two-tier trigger system selects pp collision events of interest. The first level of the trigger system, composed of custom hardware processors, uses information from the calorimeters and muon detectors to select the most interesting events in a fixed time interval of less than $4\,\mu$s. The high-level trigger processor farm further decreases the event rate from around 100 kHz to less than 1 kHz, before data storage. The CMS detector is nearly hermetic, which allows for momentum balance measurements in the plane transverse to the beam axis. A more detailed description of the CMS detector, together with a definition of the coordinate system used and the relevant kinematic variables, can be found in Ref. [54].

3   Simulated event samples

The search relies on multiple event samples, in data or generated from Monte Carlo (MC) simulations, to estimate the contributions from SM backgrounds, as described in Section 5. The SM backgrounds for the search are QCD multijet, top quark-antiquark ($t\bar{t}$), and single top production, and the associated production of jets and and a vector boson (W, $Z \to \nu\bar{\nu}$). Residual contributions from other processes, such as WW, WZ, ZZ (diboson) production and the associated production of $t\bar{t}$ and a W or Z boson, are also considered. Other processes, such as Drell–Yan ($q\bar{q} \to Z/\gamma^* \to \ell^+\ell^-$) and γ+jets production, are also relevant for some control regions, defined in Section 5.5.

The MADGRAPH5_AMC@NLO 2.2.2 [55] event generator code is used at leading-order (LO) accuracy to produce samples of W+jets, Z+jets, γ+jets, $t\bar{t}$, and multijet events. The same code is used at next-to-leading-order (NLO) accuracy to generate samples of single top quarks (both s- and t-channel production), WZ, ZZ, $t\bar{t}$W, and $t\bar{t}$Z events. The NLO POWHEG v2 [56, 57] generator is used to describe WW events and the tW-channel production of single top quark events. The simulated samples are normalised according to production cross sections that are calculated with NLO and next-to-NLO precision [55, 57–62], or with LO precision in the case of multijet and γ+jets production. The GEANT4 [63] package is used to simulate the detector response.

Event samples for signal models involving gluino or squark pair production in association with up to two additional partons are generated at LO with MADGRAPH5_AMC@NLO, and the decay of the SUSY particles is performed with PYTHIA 8.205 [64]. Inclusive, process-dependent, signal production cross sections are calculated with NLO plus next-to-leading-logarithmic (NLL) accuracy [33, 65–69]. The theoretical systematic uncertainties are typically dominated by the parton density function (PDF) uncertainties, evaluated using the CTEQ6.6 [70] and MSTW2008 [71] PDFs. The detector response for signal models is provided by the CMS fast simulation package [72].

The NNPDF3.0 LO and NLO [73] parton distribution functions (PDFs) are used, respectively, with the LO and NLO generators described above. The PYTHIA program with the CUETP8M1 underlying event tune [74] is used to describe parton showering and hadronisation for all simulated samples. To model the effects of multiple pp collisions within the same or neighbouring bunch crossings (pileup), all simulated events are generated with a nominal distribution of pp interactions per bunch crossing and then reweighted to match the pileup distribution as mea-

138 sured in data. On average, approximately fifteen different pp collisions, identifiable via their
139 primary interaction vertex, are reconstructed per event. Finally, (near-unity) corrections to the
140 normalisation of the simulated samples for the γ+jets, W($\to \mu\nu$)+jets, $t\bar{t}$, Z($\to \mu\mu$)+jets, and
141 Z($\to \nu\bar{\nu}$)+jets processes are derived using data sidebands to the control regions.

4   Event reconstruction

143 Global event reconstruction is provided by the particle flow (PF) algorithm [75, 76], designed
144 to identify each particle using an optimised combination of information from all detector sys-
145 tems. In this process, the identification of the particle type (photon, electron, muon, charged
146 hadron, neutral hadron) plays an important role in the determination of the particle direction
147 and energy.

148 Among the vertices reconstructed within 24 (2) cm of the detector centre parallel (perpendic-
149 ular) to the beam axis, the primary vertex (PV) is assigned to be the one with the largest sum
150 of charged particle (track) p_T^2 values. Charged-particle tracks associated with reconstructed
151 vertices from pileup events are not considered by the PF algorithm as part of the global event
152 reconstruction.

153 Photon candidates [77] are identified as ECAL energy clusters not linked to the extrapolation
154 of any track to the ECAL. The energy of photons is directly obtained from the ECAL measure-
155 ment, corrected for contributions from pileup events. Various quality-related criteria must be
156 satisfied in order to identify photons with high efficiency while minimising the misidentifica-
157 tion of electrons and associated bremstrahlung, jets, or ECAL noise as photons. The criteria
158 include the following: the shower shape of the energy deposition in the ECAL must be con-
159 sistent with that expected from a photon, the energy detected in the HCAL behind the photon
160 shower must not exceed 5% of the photon energy, and no matched hits in the pixel tracker must
161 be found.

162 Electron candidates [78] are identified as a track associated with an ECAL cluster compatible
163 with the track trajectory, as well as additional ECAL energy clusters from potential bremsstrahlung
164 photons emitted as the electron traverses material of the silicon tracker. The energy of electrons
165 is determined from a combination of the track momentum at the main interaction vertex, the
166 corresponding ECAL cluster energy, and the energy sum of all bremsstrahlung photons associ-
167 ated with the track. The quality criteria required for electrons are similar to those for photons,
168 with regards to the ECAL shower shape and the relative contributions to the total energy de-
169 posited in the ECAL and HCAL. Additional requirements are also made on the associated
170 track, which consider the track quality, energy-momentum matching, and compatibility with
171 the PV in terms of the transverse and longitudinal impact parameters.

172 Muon candidates [79] are identified as a track in the silicon tracker consistent with either a track
173 or several hits in the muon system. The track and hit parameters must satisfy various quality-
174 related criteria, described in Ref. [79]. The energy of muons is obtained from the corresponding
175 track momentum.

176 Charged hadrons are identified as tracks not classified as either electrons or muons. The en-
177 ergy of charged hadrons is determined from a combination of the track momentum and the
178 corresponding ECAL and HCAL energies, corrected for contributions from pileup events and
179 the response function of the calorimeters to hadronic showers. Neutral hadrons are identified
180 as HCAL energy clusters not linked to any charged-hadron trajectory, or as ECAL and HCAL
181 energy excesses with respect to the expected charged-hadron energy deposit. The energy of

182 neutral hadrons is obtained from the corresponding corrected ECAL and HCAL energy.

183 Photons are required to be isolated from other activity in the event, such as charged and neutral
184 hadrons, within a cone $\Delta R = \sqrt{(\Delta\phi)^2 + (\Delta\eta)^2} = 0.3$ around the photon trajectory, corrected
185 for contributions from pileup events and the photon itself. Electrons and muons are also re-
186 quired to be isolated from other reconstructed particles in the event, primarily to suppress
187 background contributions from semileptonic heavy-flavour decays in multijet events. The iso-
188 lation $I_{\mathrm{rel}}^{\mathrm{mini}}$ is defined as the scalar p_{T} sum of all charged and neutral hadrons, and photons,
189 within a cone around the lepton direction, divided by the lepton p_{T}. The "mini" cone radius is
190 dependent on the lepton p_{T}, primarily to identify with high efficiency the collimated daughter
191 particles of semileptonically decaying Lorentz-boosted top quarks, according to the following:
192 $R = 0.2$ and 0.05 for, respectively, $p_{\mathrm{T}} < 50\,\mathrm{GeV}$ and $p_{\mathrm{T}} > 200\,\mathrm{GeV}$, and $R = 10\,\mathrm{GeV}/p_{\mathrm{T}}$ for
193 $50 < p_{\mathrm{T}} < 200\,\mathrm{GeV}$. The variable $I_{\mathrm{rel}}^{\mathrm{mini}}$ excludes contributions from the lepton itself and pileup
194 events. The isolation for electrons and muons is required to satisfy, respectively, $I_{\mathrm{rel}}^{\mathrm{mini}} < 0.1$ and
195 0.2 for the signal region and nonleptonic control sample selection criteria. A tighter definition
196 of muon isolation I_{rel}^{μ} is used for the definition of control regions that are required to contain at
197 least one muon. The variable I_{rel}^{μ} is determined identically to $I_{\mathrm{rel}}^{\mathrm{mini}}$ except that a cone of fixed
198 radius $R = 0.4$ is assumed.

199 Electron and muon candidates identified by the PF algorithm that do not satisfy the quality
200 criteria or the $I_{\mathrm{rel}}^{\mathrm{mini}}$ isolation requirements described above, as well as charged hadrons, are
201 collectively labelled as "single isolated tracks" if they are isolated from neighbouring tracks
202 associated to the PV. The isolation $I_{\mathrm{rel}}^{\mathrm{track}}$ is defined as the scalar p_{T} sum of tracks (excluding the
203 track under consideration) within a cone $\Delta R < 0.3$ around the track direction, divided by the
204 track p_{T}. The requirement $I_{\mathrm{rel}}^{\mathrm{track}} < 0.1$ is imposed.

205 Jets are clustered from the PF candidate particles with the infrared- and collinear-safe anti-k_t
206 algorithm [80], operated with a distance parameter of 0.4. The jet momentum is determined
207 as the vectorial sum of all particle momenta in the jet, and is found in the simulation to be
208 within 5 to 10% of its true momentum over the whole p_{T} spectrum and detector acceptance. Jet
209 energy corrections, to account for pileup [81] and to establish a uniform relative response in η
210 and a calibrated absolute response in p_{T}, are derived from the simulation, and are confirmed
211 with in situ measurements using the energy balance in dijet and photon+jet events [82]. The jet
212 energy resolution is typically 15% at 10 GeV, 8% at 100 GeV, and 4% at 1 TeV, compared to about
213 40%, 12%, and 5% obtained when the calorimeters alone are used for jet clustering. All jets are
214 required to satisfy loose requirements on the relative composition of their particle constituents
215 to reject noise in the calorimeter systems or failures in event reconstruction.

216 Jets are identified as originating from b quarks using the combined secondary vertex algo-
217 rithm [83]. Control regions in data [84] are used to measure the probability of correctly identi-
218 fying jets as originating from b quarks (b tagging efficiency), and the probability of misidenti-
219 fying jets originating from light-flavour partons (u, d, s quarks or gluons) or a charm quark as
220 a b-tagged jet (the light-flavour and charm mistag probabilities). A working point is employed
221 that yields a b tagging efficiency of 65%, and charm and light-flavour mistag probabilities of
222 approximately 12 and 1%, respectively, for jets with p_{T} that is typical of $\mathrm{t\bar{t}}$ events.

223 An estimator of $\vec{p}_{\mathrm{T}}^{\mathrm{miss}}$ is given by the projection on the plane perpendicular to the beams of the
224 negative vector sum of the momenta of all candidate particles in an event [85], as determined
225 by the PF algorithm. Its magnitude is referred to as $E_{\mathrm{T}}^{\mathrm{miss}}$.

5   Event selection

The kinematic selection criteria used to define the signal region, containing a sample of candidate signal events, as well as a number of control regions in data, are described below. The criteria are based on the particle candidates defined by the event reconstruction algorithms described in Section 4.

5.1   Common preselection criteria

A number of beam- and detector-related effects, such as beam halo, reconstruction failures, spurious detector noise, or event misreconstruction due to detector inefficiencies, can lead to events with anomalous levels of activity. These events, which can exhibit large, nonphysical values of E_T^{miss}, are rejected with high efficiency by applying a range of dedicated vetoes [85, 86].

In order to suppress SM processes with genuine $\vec{p}_T^{\,miss}$ from neutrinos, events containing an isolated electron or muon that satisfies $p_T > 10\,\mathrm{GeV}$ and $|\eta| < 2.5$ are vetoed. Events containing an isolated photon with $p_T > 25\,\mathrm{GeV}$ and $|\eta| < 2.5$ are also vetoed, in order to select only multijet final states. Furthermore, events containing a single isolated track satisfying $p_T > 10\,\mathrm{GeV}$ and $|\eta| < 2.5$ are vetoed in order to reduce the background contribution from final states containing hadronically decaying tau leptons.

Each jet j_i considered by this search is required to satisfy $p_T^{j_i} > 40\,\mathrm{GeV}$ and $|\eta^{j_i}| < 3$. The number of jets within this experimental acceptance is labelled henceforth as n_{jet}. The highest p_T jet in the event is required to have $p_T^{j_1} > 100\,\mathrm{GeV}$ and $|\eta^{j_1}| < 2.5$. The second-highest p_T jet in the event is used to categorise events, as described in Section 5.2. If the jet satisfies $p_T^{j_2} > 100\,\mathrm{GeV}$, then this category of events is labelled "symmetric" and targets primarily topologies resulting from pair-produced SUSY particles. If the jet satisfies $40 < p_T^{j_2} < 100\,\mathrm{GeV}$ then the event is labelled as "asymmetric," and if there exists no second jet with $p_T^{j_2} > 40\,\mathrm{GeV}$, the event is labelled monojet. The asymmetric and monojet topologies target models involving the direct production of stable, weakly interacting, massive particles. The mass scale of the physics processes being probed is characterised by the scalar p_T sum of the jets, defined as $H_T = \sum_{i=1}^{n_{jet}} p_T^{j_i}$. The magnitude of the vector $\vec{p}_T$ sum of these jets, defined by $H_T^{miss} = |\sum_{i=1}^{n_{jet}} \vec{p}_T^{\,j_i}|$, is used to identify events with significant imbalance in $\vec{p}_T^{\,miss}$. Events are vetoed if any jet satisfies $p_T > 40\,\mathrm{GeV}$ and $|\eta| > 3$ to ensure that jets reconstructed in the forward regions of the detector do not contribute significantly to H_T^{miss}.

The dimensionless variable H_T^{miss}/E_T^{miss} is used to remove events that contain several jets with transverse momenta below the jet p_T thresholds but an appreciable vector p_T sum so as to contribute significantly to H_T^{miss} relative to E_T^{miss}. This background is typical of multijet events, which is suppressed by requiring $H_T^{miss}/E_T^{miss} < 1.25$. The requirement is imposed as part of the common preselection criteria used to define all control samples to minimise potential systematic biases associated with the simulation modelling for this variable. A high efficiency is maintained for SM or new-physics processes that produce unobserved particles, which are characterised by large values of $\vec{p}_T^{\,miss}$ and values of H_T^{miss}/E_T^{miss} close to unity.

Significant jet activity and $\vec{p}_T^{\,miss}$ in the event is ensured by requiring $H_T > 200\,\mathrm{GeV}$ and $H_T^{miss} > 130\,\mathrm{GeV}$, respectively. These requirements complete the common preselection criteria, summarised in Table 1, used to define a sample of all-jet events characterised by high jet activity and appreciable $\vec{p}_T^{\,miss}$.

Table 1: Summary of the event selection criteria and categorisation used to define the signal and control regions.

Common preselection	
E_T^{miss} quality	Filters related to beam and instrumental effects, and reconstruction failures
Lepton/photon vetoes	$p_T > 10, 10, 25\,\mathrm{GeV}$ for isolated tracks, leptons, photons (respectively) and $|\eta| < 2.5$
Jet j_i acceptance	Consider each jet j_i that satisfies $p_T^{j_i} > 40\,\mathrm{GeV}$ and $|\eta^{j_i}| < 3$
Jet j_1 acceptance	$p_T^{j_1} > 100\,\mathrm{GeV}$ and $|\eta^{j_1}| < 2.5$
Jet j_2 acceptance	$p_T^{j_2} < 40\,\mathrm{GeV}$ (monojet), $40 < p_T^{j_2} < 100\,\mathrm{GeV}$ (asymmetric), $p_T^{j_2} > 100\,\mathrm{GeV}$ (symmetric)
Forward jet veto	Veto events containing a jet satisfying $p_T > 40\,\mathrm{GeV}$ and $|\eta| > 3$
Jets below threshold	$H_T^{miss} / E_T^{miss} < 1.25$
Energy sums	$H_T > 200\,\mathrm{GeV}$ and $H_T^{miss} > 130\,\mathrm{GeV}$
Event categorisation	
n_{jet}	1 (monojet), 2, 3, 4, ≥ 5 (asymmetric), 2, 3, 4, ≥ 5 (symmetric)
n_b	0, 1, 2, ≥ 3 ($n_b \leq n_{jet}$)
H_T (GeV)	200, 250, 300, 350, 400, 500, 600, $> 800\,\mathrm{GeV}$ (bins can be dropped/merged *vs.* n_{jet}, Table 2)
Signal region (SR)	Preselection +
QCD multijet rejection	$\alpha_T > 0.65, 0.60, 0.55, 0.53, 0.52, 0.52, 0.52$ (mapped to H_T bins in range $200 < H_T < 800\,\mathrm{GeV}$)
QCD multijet rejection	$\Delta\phi_{min}^* > 0.5$ ($n_{jet} \geq 2$) or $\Delta\phi_{min}^{*25} > 0.5$ ($n_{jet} = 1$)
Control regions (CR)	Preselection +
Multijet-enriched	SR + $H_T^{miss} / E_T^{miss} > 1.25$ (inverted)
γ+jets	1γ with $p_T > 200\,\mathrm{GeV}$, $|\eta| < 1.45$, $\Delta R(\gamma, j_i) > 1.0$, $H_T > 400\,\mathrm{GeV}$, same α_T req. as SR
μ+jets	1μ with $p_T > 30\,\mathrm{GeV}$, $|\eta| < 2.1$, $I_{rel}^\mu < 0.1$, $\Delta R(\mu, j_i) > 0.5$, $30 < m_T(\vec{p}_T^\mu, \vec{p}_T^{miss}) < 125\,\mathrm{GeV}$
$\mu^\pm\mu^\mp$+jets	2μ with $p_T > 30\,\mathrm{GeV}$, $|\eta| < 2.1$, $I_{rel}^\mu < 0.1$, $\Delta R(\mu_{1,2}, j_i) > 0.5$, $|m_{\mu\mu} - m_Z| < 25\,\mathrm{GeV}$

5.2 Event categorisation

Events selected by the common preselection criteria are categorised according to n_{jet}, the number of b-tagged jets n_b, and H_T. Nine categories in n_{jet} are employed: the monojet topology ($n_{jet} = 1$) and four n_{jet} bins (2, 3, 4, ≥ 5) for each of the asymmetric and symmetric topologies. Events are also categorised by n_b (0, 1, 2, ≥ 3), where n_b is bounded from above by n_{jet}, resulting in 32 categories in terms of both n_{jet} and n_b. For each (n_{jet}, n_b) category, events are binned according to H_T: four $50\,\mathrm{GeV}$ bins at low jet activity in the range $200 < H_T < 400\,\mathrm{GeV}$, two $100\,\mathrm{GeV}$ bins in the range $400 < H_T < 600\,\mathrm{GeV}$, one bin covering the region $600 < H_T < 800\,\mathrm{GeV}$, and a final open bin for $H_T > 800\,\mathrm{GeV}$. These categorisations are summarised in Table 1. The H_T binning scheme is adapted independently per (n_{jet}, n_b) category by removing or merging bins to satisfy a threshold on the minimum number of data events in the control regions, which are used to estimate SM backgrounds, provide checks, and validate assumptions within the methods. The lower bounds of the first and final (open) bins in H_T are summarised in Table 2. In summary, the search employs a categorisation scheme for events that results in 191 bins, defined in terms of n_{jet}, n_b, and H_T.

5.3 Signal region

For events satisfying the common preselection criteria described above, the multijet background dominates over all other SM backgrounds. Several variables are employed to reduce the multijet contribution to a low level with respect to other SM backgrounds.

The dimensionless kinematic variable α_T [28, 53], defined in Eq. (2) below, is used to provide discrimination against multijet events that do not contain significant $\vec{p}_T^{miss}$ or that contain large $\vec{p}_T^{miss}$ only because of p_T mismeasurements, while retaining sensitivity to new-physics events with significant $\vec{p}_T^{miss}$. The α_T variable depends solely on the transverse component of jet four-

Table 2: Summary of the lower bounds of the first and final bins in H_T [GeV] (the latter in parentheses) as a function of n_{jet} and n_b.

$n_{jet} \setminus n_b$	0	1	2	≥ 3
Monojet				
1	200 (600)	200 (500)	-	-
Asymmetric				
2	200 (600)	200 (500)	200 (400)	-
3	200 (600)	200 (600)	200 (500)	200 (300)
4	200 (600)	200 (600)	200 (600)	250 (400)
≥ 5	250 (600)	250 (600)	250 (600)	300 (500)
Symmetric				
2	200 (800)	200 (800)	200 (600)	-
3	200 (800)	250 (800)	250 (800)	- (250)
4	300 (800)	300 (800)	300 (800)	300 (800)
≥ 5	350 (800)	350 (800)	350 (800)	350 (800)

momenta and is intrinsically robust against the presence of jet energy mismeasurements in multijet systems. For events containing only two jets, α_T is defined as $\alpha_T = E_T^{j_2}/M_T$, where $E_T = E \sin\theta$, where E is the energy of the jet and θ is its polar angle with respect to the beam axis, $E_T^{j_2}$ is the transverse energy of the jet with smaller E_T, and M_T is the transverse mass of the dijet system, defined as:

$$M_T = \sqrt{\left(\sum_{i=1}^{2} E_T^{j_i}\right)^2 - \left(\sum_{i=1}^{2} p_x^{j_i}\right)^2 - \left(\sum_{i=1}^{2} p_y^{j_i}\right)^2},$$ (1)

where $E_T^{j_i}$, $p_x^{j_i}$, and $p_y^{j_i}$ are, respectively, the transverse energy, and the x and y components of the transverse momentum of jet j_i. For a perfectly measured dijet event with $E_T^{j_1} = E_T^{j_2}$ and back-to-back jets ($\Delta\phi = \pi$), and in the limit in which the momentum of each jet is large compared with its mass, the value of α_T is 0.5. For an imbalance in the E_T of back-to-back jets, α_T is reduced to a value < 0.5, which gives the variable its intrinsic robustness. Values significantly greater than 0.5 are observed when the two jets are not back-to-back and recoil against $\vec{p}_T^{\text{miss}}$ from weakly interacting particles that escape the detector.

The definition of the α_T variable can be generalised for events with more than two jets [28]. The mass scale for any process is characterised through the scalar sum of the jet transverse energies, defined as $\mathcal{E}_T = \sum_{i=1}^{N_{jet}} E_T^{j_i}$, where N_{jet} is the number of jets with E_T above a predefined threshold. (The definition of $\mathcal{E}_T$ should be contrasted with that of H_T, the scalar p_T sum of the jets.) For events with three or more jets, a pseudo-dijet system is formed by combining the jets in the event into two pseudo-jets. The $\mathcal{E}_T$ for each of the two pseudo-jets is given by the scalar E_T sum of its contributing jets. The combination chosen is the one that minimises $\Delta\mathcal{E}_T$, defined as the difference between these sums for the two pseudo-jets. This clustering criterion assumes a balanced-event hypothesis, which provides strong separation between SM multijet events and events with genuine $\vec{p}_T^{\text{miss}}$. The α_T definition can be generalised to:

$$\alpha_T = \frac{1}{2}\frac{\mathcal{E}_T - \Delta\mathcal{E}_T}{\sqrt{(\mathcal{E}_T)^2 - (H_T^{\text{miss}})^2}}.$$ (2)

When jet energies are mismeasured, or there are neutrinos from heavy-flavour quark decays,

the magnitudes of H_T^{miss} and $\Delta\mathcal{E}_T$ are highly correlated. This correlation is much weaker for R-parity-conserving SUSY events, where each of the two decay chains produces an undetected LSP.

Multijet events populate the region $\alpha_T < 0.5$ and the α_T distribution is characterised by a sharp edge at 0.5, beyond which the multijet event yield falls by several orders of magnitude. Multijet events with extremely rare but large stochastic fluctuations in the calorimetric measurements of jet energies can lead to values of α_T slightly above 0.5. The edge at 0.5 sharpens with increasing H_T for events containing at least three jets, primarily due to a corresponding increase in the average jet energy and consequently a (relative) improvement in the jet energy resolution.

For events containing at least two jets, thresholds on the minimum allowed α_T values are applied independent of n_{jet} and n_b but dependent on H_T, for events that satisfy $200 < H_T < 800\,\text{GeV}$. The α_T thresholds vary between 0.65 to 0.52 for, respectively, the regions $200 < H_T < 250\,\text{GeV}$ and $400 < H_T < 800\,\text{GeV}$. No requirement on α_T is made for the region $H_T > 800\,\text{GeV}$. The thresholds employed are summarised in Table 1. The α_T thresholds are motivated both by the trigger conditions used to record the candidate signal events, described below, and by simulation-based studies and estimates of the multijet background derived from data.

An additional variable is based on the minimum azimuthal separation between a jet and the negative vector $\vec{p}_T$ sum derived from all other jets in the event [28],

$$\Delta\phi_{min}^* = \min_{\forall j_k \in [1, n_{jet}]} \Delta\phi \left(\vec{p}_T^{j_k}, -\sum_{\substack{j_i = 1 \\ j_i \neq j_k}}^{n_{jet}} \vec{p}_T^{j_i} \right). \tag{3}$$

This variable discriminates between final states with genuine $\vec{p}_T^{miss}$, e.g. from the leptonic decay of the W boson, and energetic multijet events that have significant $\vec{p}_T^{miss}$ through jet energy mismeasurements or through the production of neutrinos, collinear with the axis of a jet, from semileptonic heavy-flavour decays. Multijet events populate the region $\Delta\phi_{min}^* < 0.5$, with the multijet distribution peaking at a value of zero and falling approximately exponentially over five orders of magnitude to a single-event level at a value of $\Delta\phi_{min}^* \approx 0.5$, which is close to the distance parameter value of 0.4 used by the anti-k_t jet clustering algorithm. Events with a genuine source of $\vec{p}_T^{miss}$ exhibit a long tail in $\Delta\phi_{min}^*$ with values as large as π.

A requirement of $\Delta\phi_{min}^* > 0.5$ is sufficient to effectively suppress the multijet background to a low level while maintaining high efficiency for new-physics signatures. The combined rejection power of the α_T and $\Delta\phi_{min}^*$ requirements for the region $200 < H_T < 800\,\text{GeV}$ is sufficient to suppress multijet events to the few percent level (and always $< 10\%$) with respect to all other SM backgrounds in all H_T bins for all event categories of the signal region. For the region $H_T > 800\,\text{GeV}$, a similar control of the multijet background is achieved solely with the $\Delta\phi_{min}^* > 0.5$ requirement.

Figure 1 shows the distributions of α_T and $\Delta\phi_{min}^*$ observed in data for events that satisfy $n_{jet} \geq 2$ and all other selection criteria that define the signal region, summarised in Table 1, as well as the following modifications. In the case of the α_T distribution, the events that satisfy $\alpha_T < 0.55$ must fulfill only the common preselection criteria defined in Table 1, and no H_T^{miss} requirement is made. Further, all events are required to satisfy $H_T > 300\,\text{GeV}$. In the case of the $\Delta\phi_{min}^*$ distribution, the only additional requirement is $H_T > 800\,\text{GeV}$. For both distributions, the events are recorded with a set of inclusive trigger conditions that are independent of the α_T and $\Delta\phi_{min}^*$ variables. The distributions for the QCD multijet background are determined from
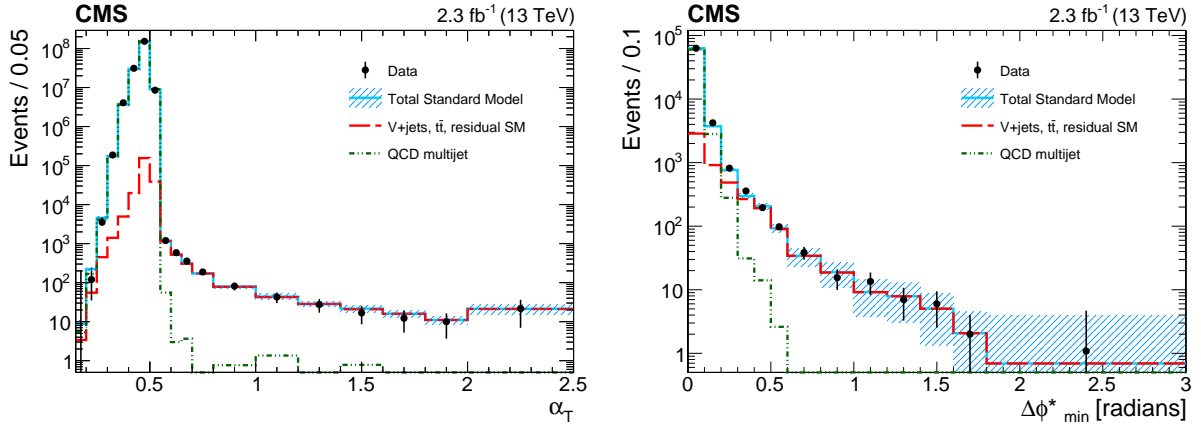
Figure 1: The (left) α_T and (right) $\Delta\phi^*_{min}$ distributions observed in data for events that satisfy the selection criteria defined in the text. The statistical uncertainties for the multijet and SM expectations are represented by the hatched areas (visible only for statistically limited bins). The final bin of each distribution contains the overflow events.

355 simulation while all other SM backgrounds (vector boson production in association with jets,
356 $t\bar{t}$, and other residual contributions from rare SM processes) are estimated using a μ+jets data
357 control sample, described in Section 6.2. The contribution from multijet events is observed to
358 fall by more than five orders of magnitude for both variables.

359 The α_T and $\Delta\phi^*_{min}$ requirements described above, in conjunction with the common preselection
360 requirements $H_T^{miss} > 130\,\text{GeV}$ and $H_T^{miss}/E_T^{miss} < 1.25$, provide strong rejection power against
361 the multijet background for events that satisfy $n_{jet} \geq 2$. For monojet events, a modification
362 to the $\Delta\phi^*_{min}$ variable, which considers soft jets with $p_T > 25\,\text{GeV}$ ($\Delta\phi^{*25}_{min}$), is utilised. No α_T
363 requirement is imposed, and $\Delta\phi^{*25}_{min} > 0.5$ is sufficient to suppress contributions from multijet
364 events to a negligible level. The aforementioned requirements complete the event selection
365 criteria for the signal region.

366 Finally, $\Delta\phi^{*25}_{min}$ is also used as a control variable for events that satisfy $n_{jet} \geq 2$ to identify multijet
367 contributions arising from instrumental effects, such as inefficient detector elements or detector
368 noise. The axis of any jet that satisfies $\Delta\phi^{*25}_{min} < 0.5$ is used to identify localised behaviour in
369 the (η, ϕ) plane, which may be indicative of instrumental defects. No significant anomalies are
370 observed in the sample of candidate signal events following the application of the dedicated
371 vetoes described in Section 5.1.

372 Multiple trigger conditions are employed in combination to record signal candidate events. A
373 set of trigger conditions utilise calculations of both H_T and α_T to record events with two or more
374 jets. An event is recorded if it satisfies any of the following pairs of (H_T [GeV], α_T) thresholds,
375 (200, 0.57), (250, 0.55), (300, 0.53), (350, 0.52), or (400, 0.51), as well as a requirement on the mean
376 value of the two highest p_T jets, $\langle p_T^{j1} + p_T^{j2} \rangle > 90\,\text{GeV}$. These requirements are collectively
377 labelled as the "H_T–α_T" triggers. In addition, candidate signal events with one or more jets are
378 also recorded if they satisfy the requirements $H_T^{miss} > 90\,\text{GeV}$ and $E_T^{miss} > 90\,\text{GeV}$. Finally, for
379 events that satisfy $H_T > 800\,\text{GeV}$, an additional trigger condition, defined by $H_T > 800\,\text{GeV}$, is
380 employed in addition to the H_T–α_T trigger requirements to record events characterised by high
381 activity in the calorimeters with high efficiency. The trigger-level jet energies are corrected
382 to account for energy scale and pileup effects. The aforementioned triggers are employed in
383 combination to provide efficiencies at or near 100% for all bins in the signal region.

5.4 Using $H_{\mathrm{T}}^{\mathsf{miss}}$ templates

Following the event selection criteria described above, which provide a sample of signal candidate events with a negligible contribution from multijet events, further discriminating power is required to separate new-physics signatures from the remaining SM backgrounds, which are dominated by the production of $t\bar{t}$ or $W(\to\ell\nu)$+jets and $Z(\to\nu\bar{\nu})$+jets events. Given that the characteristic signature of SUSY production at the LHC is a final state of multijets accompanied by large values of $\vec{p}_{\mathrm{T}}^{\mathrm{miss}}$ from the LSPs, the search exploits the use of the $H_{\mathrm{T}}^{\mathrm{miss}}$ variable as an additional discriminant between new-physics and SM processes.

The search relies directly on simulation to determine a template for each (n_{jet}, n_{b}, H_{T}) bin that describes the expected distribution of events as a function of $H_{\mathrm{T}}^{\mathrm{miss}}$. These templates are used by the likelihood function as a model for the data, details of which can be found in Section 7. The templates are extensively validated against data in multiple control regions, and these studies are used to establish the uncertainty in the simulation modelling of the $H_{\mathrm{T}}^{\mathrm{miss}}$ variable. The effects of theoretical and experimental uncertainties on the $H_{\mathrm{T}}^{\mathrm{miss}}$ distributions are also studied. Further details can be found in Section 6.2.

5.5 Control regions

Four control regions in data are employed to estimate the background contributions from SM processes, which modify and expand the common preselection criteria described above according to the descriptions found below and summarised in Table 1. The first control region comprises a multijet-enriched sample of events, and is defined by the signal region selection criteria and the inverted requirement $H_{\mathrm{T}}^{\mathrm{miss}}/E_{\mathrm{T}}^{\mathrm{miss}} > 1.25$. The events are recorded with the signal triggers described above, and the sample is used to estimate the multijet background in the signal region. Three additional control regions, defined by inverting one of the photon or lepton vetoes to select samples of γ+jets, μ+jets, or $\mu\mu$+jets events, are used to estimate the background contributions from SM processes with final states containing genuine $\vec{p}_{\mathrm{T}}^{\mathrm{miss}}$, which are primarily $t\bar{t}$, $W(\to\ell\nu)$+jets, and $Z(\to\nu\bar{\nu})$+jets.

Additional kinematic requirements are employed to ensure the control samples are enriched in the same SM processes that contribute to background events in the signal region, and are depleted in contributions from multijet production or a wide variety of SUSY models (i.e. so-called signal contamination). The samples are defined, and their events are identically categorised and binned, such that the kinematic properties of events in the control regions and the signal candidate events resemble as closely as possible one another once the photon, muon, or dimuon system is ignored in the calculation of quantities such as H_{T} and $H_{\mathrm{T}}^{\mathrm{miss}}$. The selections are summarised in Table 1 and described below.

The γ+jets event sample is defined by the common preselection requirements, but the photon veto is inverted and each event is required to contain a single isolated photon, as defined in Section 4, that satisfies $p_{\mathrm{T}} > 200\,\mathrm{GeV}$ and $|\eta| < 1.45$ and is well separated from each jet $\mathrm{j_i}$ in the event according to $\Delta R(\gamma, \mathrm{j_i}) > 1.0$. In addition, events must satisfy $H_{\mathrm{T}} > 400\,\mathrm{GeV}$, as well as the same H_{T}-dependent α_{T} requirements used to define the signal region. The events are recorded using a single-photon trigger condition and the selection criteria result in a trigger efficiency of $\gtrsim 99\%$.

The μ+jets event sample is defined by the common preselection requirements, but the muon veto is inverted and each event is required to contain a single isolated muon, as defined in Section 4, that satisfies $p_{\mathrm{T}} > 30\,\mathrm{GeV}$ and $|\eta| < 2.1$ and is well separated from each jet $\mathrm{j_i}$ in the event according to $\Delta R(\mu, \mathrm{j_i}) > 0.5$. The transverse mass formed by the muon p_{T} and $\vec{p}_{\mathrm{T}}^{\mathrm{miss}}$

system must satisfy $30 < m_T < 125\,\text{GeV}$ to select a sample of events rich in W bosons, produced promptly or from the decay of top quarks. The $\mu\mu$+jets sample uses a similar set of selection criteria as the μ+jets sample, but specifically requires two oppositely charged isolated muons that both satisfy $p_T > 30\,\text{GeV}$ and $|\eta| < 2.1$ and are well separated from the jets in the event ($\Delta R(\mu_{1,2}, j_i) > 0.5$). The muons are also required to have a dilepton invariant mass within a $\pm 25\,\text{GeV}$ window around the nominal mass of the Z boson [9]. For both the muon and dimuon samples, no requirement is made on α_T in order to increase the statistical precision of the predictions from these samples. Both the μ+jets and $\mu\mu$+jets samples are recorded using a trigger that requires an isolated muon. The selection criteria of the μ+jets and $\mu\mu$+jets event samples are chosen so that the trigger is maximally efficient, with values of $\sim$90% and $\sim$99%, respectively.

6   Estimation of backgrounds

6.1   Multijet background

The signal region is defined in a manner that suppresses the expected contribution from multijet production to a low level with respect to the total expected background from other SM processes for all signal region bins. This is achieved primarily through the application of very tight requirements on the variables α_T and $\Delta\phi^*_{\text{min}}$, as described in Section 5.3, as well as the requirement $H_T^{\text{miss}}/E_T^{\text{miss}} < 1.25$. In this section, we discuss these requirements further, and present the estimate of the multijet background.

The contamination from multijet events in the signal region is estimated using a multijet-enriched data sideband to the signal region, defined by the (inverted) requirement $H_T^{\text{miss}}/E_T^{\text{miss}} > 1.25$. The observed counts in data, categorised according to n_{jet} and H_T, are corrected to account for contamination from nonmultijet SM processes, and the corrected counts $\mathcal{N}^{\text{data}}(n_{\text{jet}}, H_T)$ are assumed to arise solely from QCD multijet production. The nonmultijet processes, which comprise vector boson and $t\bar{t}$ production and residual contributions from other SM processes, are estimated using the μ+jets control region, as described in Section 6.2.

Independent ratios $\mathcal{R}^{\text{QCD}}(n_{\text{jet}}, H_T)$ of the number of multijet events that satisfy the requirement $H_T^{\text{miss}}/E_T^{\text{miss}} < 1.25$ to the number that fail are determined from simulation for events categorised according to n_{jet} and H_T, and inclusively with respect to n_b and H_T^{miss}. The product of each ratio $\mathcal{R}^{\text{QCD}}(n_{\text{jet}}, H_T)$ and the corresponding corrected data count $\mathcal{N}^{\text{data}}(n_{\text{jet}}, H_T)$ provides the estimate of the multijet background $\mathcal{P}(n_{\text{jet}}, H_T)$. The distributions of the predicted event counts $\mathcal{P}(n_{\text{jet}}, H_T)$ as a function of n_b and H_T^{miss} are implemented with the multiplier terms $\mathcal{K}_{n_{\text{jet}}, H_T}(n_b, H_T^{\text{miss}})$, and are assumed to be identical to the distributions expected for the nonmultijet backgrounds. This final assumption is based on studies in simulation and is a valid approximation given the magnitude of the statistical and systematic uncertainties in the ratios $\mathcal{R}^{\text{QCD}}(n_{\text{jet}}, H_T)$, as described below. Assuming i, j, k, and l are the bin indices for, respectively, n_{jet}, H_T, n_b, and H_T^{miss}:

$$\mathcal{P}(i, j, k, l) = \mathcal{N}^{\text{data}}(i, j)\,\mathcal{R}^{\text{QCD}}(i, j)\,\mathcal{K}_{i,j}(k, l). \tag{4}$$

The use of simulation to determine $\mathcal{R}^{\text{QCD}}(n_{\text{jet}}, H_T)$ is validated using a multijet-enriched data sideband defined by $\Delta\phi^*_{\text{min}} < 0.5$. Each ratio $\mathcal{R}^{\text{data}}(n_{\text{jet}}, H_T)$ is constructed from data counts, corrected to account for contributions from nonmultijet processes, and compared with the corresponding ratio $\mathcal{R}^{\text{QCD}}(n_{\text{jet}}, H_T)$, determined from simulation, through the double ratio $\mathcal{R}^{\text{data}}/\mathcal{R}^{\text{QCD}}$, as shown in Fig. 2. The double ratios are statistically compatible with unity across
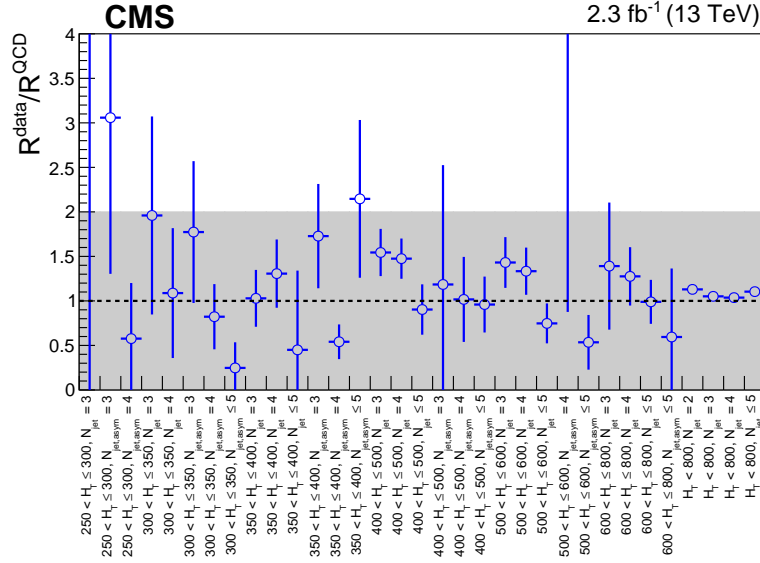
Figure 2: Validation of the ratio $\mathcal{R}^{QCD}$ determined from simulation in bins of n_{jet} and H_T [GeV] by comparing with an equivalent ratio $\mathcal{R}^{data}$ constructed from data in a multijet-enriched sideband to the signal region. A value of unity is expected for the double ratio $\mathcal{R}^{data}/\mathcal{R}^{QCD}$, and the grey shaded band represents the assumed systematic uncertainty of 100% in $\mathcal{R}^{QCD}$.

the full phase space of the signal region, including the bins at high H_T, which exhibit the highest statistical precision. In addition to statistical uncertainties as large as $\sim$100%, a systematic uncertainty of 100% in $\mathcal{R}^{QCD}$ is assumed to adequately cover the observed level of agreement for the full signal region phase space, as well as any limitations in the assumptions concerning $\mathcal{K}_{n_{jet},H_T}(n_b, H_T^{miss})$ for all event categories defined in terms of n_{jet} and H_T.

6.2 Backgrounds with genuine E_T^{miss}

Following the suppression of multijet events through the use of the α_T and $\Delta\phi_{min}^*$ variables, the dominant nonmultijet backgrounds involve SM processes that produce high-p_T neutrinos in the final state. In events with few jets or few b quark jets, the associated production of W or Z bosons and jets, with the decays $W^\pm \to \ell\nu$ ($\ell = $ e, μ, τ) or $Z \to \nu\bar{\nu}$, dominate the background counts. For W boson decays that yield an electron or muon (possibly originating from leptonic τ decays), the background contributions result from events containing an e or μ that are not rejected by the lepton vetoes. The veto of events containing at least one isolated track further suppresses these backgrounds, including those from single-prong τ-lepton decays. At higher jet or b-quark jet multiplicities, single top quark and $t\bar{t}$ production, followed by semileptonic top quark decay, also become an important source of background.

The method to estimate the nonmultijet backgrounds in the signal region relies on the use of a transfer ($\mathcal{T}$) factor determined from simulation that is constructed per bin (in terms of n_{jet}, n_b, and H_T) per control region. Each $\mathcal{T}$ factor is defined as the ratio of the expected yields in the same (n_{jet}, n_b, H_T) bins of the signal region $\mathcal{N}_{MC}^{SR}$ and one of the control regions $\mathcal{N}_{MC}^{CR}$. The $\mathcal{T}$ factors are used to extrapolate from the event yields observed in each bin of a data control sample $\mathcal{N}_{data}^{CR}$ to provide an estimate for the background, integrated over H_T^{miss}, from a particular SM process or processes in the corresponding bin of the signal region $\mathcal{N}_{data}^{SR}$. The superscript SR or CR refers to, respectively, the process or processes being estimated and one of the μ+jets, $\mu\mu$+jets, and γ+jets control regions, described in Section 5.5. The subscript refers

to whether the counts are obtained from data, simulation ("MC"), or an estimate ("pred").

The method aims to minimise the effects of simulation mismodelling, as many systematic biases in the simulation are expected to largely cancel in the $\mathcal{T}$ factors, given that the events in any given (n_jet, n_b, H_T) bin of the control regions closely mirror those in the corresponding bin in the signal region in terms of the event scale, topology, and kinematics, and the relative background compositions. In short, minimal extrapolations are made. Uncertainties in the $\mathcal{T}$ factors are determined from data, as described below.

Three independent estimates of the irreducible background of $Z \to \nu\bar{\nu}$ + jets events are determined from the γ+jets, $\mu\mu$+jets, and μ+jets data control samples. The γ+jets and $Z \to \mu\mu$ + jets processes have similar kinematic properties when the photon or muons are ignored [87], albeit different acceptances. In addition, the γ+jets process has a larger production cross section than $Z \to \nu\bar{\nu}$ + jets events. The μ+jets data sample is used to provide an estimate for both the $Z \to \nu\bar{\nu}$ + jets background, as well as the other dominant SM processes, $t\bar{t}$ and W boson production (labelled collectively as W/$t\bar{t}$). Residual contributions from all other SM relevant processes, such as single top quark, diboson, and Drell–Yan production, are also included as part of the W/$t\bar{t}$ estimate from the μ+jets sample. The definition of the various $\mathcal{T}$ factors used in the search are given below:

$$\mathcal{N}_\text{pred}^\text{W/t\bar{t}} = \mathcal{T}_{\mu+\text{jets}}^\text{W/t\bar{t}}\, \mathcal{N}_\text{data}^{\mu+\text{jets}}, \qquad\qquad \mathcal{T}_{\mu+\text{jets}}^\text{W/t\bar{t}} = \left(\frac{\mathcal{N}_\text{MC}^\text{W/t\bar{t}}}{\mathcal{N}_\text{MC}^{\mu+\text{jets}}} \right); \tag{5}$$

$$\mathcal{N}_\text{pred}^{Z\to\nu\bar{\nu}} = \mathcal{T}_{\mu+\text{jets}}^{Z\to\nu\bar{\nu}}\, \mathcal{N}_\text{data}^{\mu+\text{jets}}, \qquad\qquad \mathcal{T}_{\mu+\text{jets}}^{Z\to\nu\bar{\nu}} = \left(\frac{\mathcal{N}_\text{MC}^{Z\to\nu\bar{\nu}}}{\mathcal{N}_\text{MC}^{\mu+\text{jets}}} \right); \tag{6}$$

$$\mathcal{N}_\text{pred}^{Z\to\nu\bar{\nu}} = \mathcal{T}_{\mu\mu+\text{jets}}^{Z\to\nu\bar{\nu}}\, \mathcal{N}_\text{data}^{\mu\mu+\text{jets}}, \qquad\qquad \mathcal{T}_{\mu\mu+\text{jets}}^{Z\to\nu\bar{\nu}} = \left(\frac{\mathcal{N}_\text{MC}^{Z\to\nu\bar{\nu}}}{\mathcal{N}_\text{MC}^{\mu\mu+\text{jets}}} \right); \tag{7}$$

$$\mathcal{N}_\text{pred}^{Z\to\nu\bar{\nu}} = \mathcal{T}_{\gamma+\text{jets}}^{Z\to\nu\bar{\nu}}\, \mathcal{N}_\text{data}^{\gamma+\text{jets}}, \qquad\qquad \mathcal{T}_{\gamma+\text{jets}}^{Z\to\nu\bar{\nu}} = \left(\frac{\mathcal{N}_\text{MC}^{Z\to\nu\bar{\nu}}}{\mathcal{N}_\text{MC}^{\gamma+\text{jets}}} \right). \tag{8}$$

The likelihood function, described in Section 7, encodes the estimate via the $\mathcal{T}$ factors of the W/$t\bar{t}$ background, as well as the three independent estimates of the $Z \to \nu\bar{\nu}$ background, which are considered simultaneously.

Several sources of uncertainty in the $\mathcal{T}$ factors are evaluated. The most relevant effects are discussed below, and generally fall into one of two categories. The first category concerns uncertainties in the "scale factor" corrections applied to simulation, which are determined using inclusive data samples that are defined by loose selection criteria, to account for the mismodelling of theoretical and experimental parameters. The second category concerns "closure tests" in data that probe various aspects of the accuracy of the simulation to model correctly the $\mathcal{T}$ factors in the phase space of this search.

The uncertainties in the $\mathcal{T}$ factors are studied for variations in scale factors related to the jet energy scale (that result in uncertainties in the $\mathcal{T}$ factors as large as $\sim$15%), the efficiency and misidentification probability of b quark jets (up to 5%), and the efficiency to identify well-reconstructed, isolated leptons (up to $\sim$5%). A 5% uncertainty in the total inelastic cross section, $\sigma_\text{in} = 69.0 \pm 3.5$ mb [88], is assumed and propagated through to the reweighting procedure to account for differences between the simulated measured pileup, which results in changes of up to $\sim$10%. The modelling of the transverse momentum of top quarks (p_T^t) is evaluated by

comparing the simulated and measured p_T spectra of reconstructed top quarks in $t\bar{t}$ events [89]. Simulated events are reweighted according to scale factors that decrease from a value of $\sim$1.2 to $\sim$0.7, with uncertainties of $\sim$10–20%, within the range $p_T^t < 400\,\mathrm{GeV}$. The systematic uncertainties in $\mathcal{T}_{\mu+\mathrm{jets}}^{W/t\bar{t}}$ arising from variations in the p_T^t scale factors are typically small ($\lesssim 5\%$), due to the comparable phase space probed by the signal and control regions, while larger uncertainties ($\lesssim 20\%$) in $\mathcal{T}_{\mu+\mathrm{jets}}^{Z\to\nu\bar{\nu}}$ are observed due to the potential for significant contamination from $t\bar{t}$ when using $W(\to \ell\nu)$+jets to predict $Z(\to\nu\bar{\nu})$+jets.

Table 3: Systematic uncertainties (in percent) in the transfer ($\mathcal{T}$) factors used in the method to estimate the SM backgrounds with genuine $\vec{p}_T^{\,miss}$ in the signal region. The quoted ranges provide representative values of the observed variations as a function of n_{jet} and H_T.

Systematic source	Uncertainty in $\mathcal{T}$ factor [%]			
	$\mathcal{T}_{\mu+\mathrm{jets}}^{W/t\bar{t}}$	$\mathcal{T}_{\mu+\mathrm{jets}}^{Z\to\nu\bar{\nu}}$	$\mathcal{T}_{\mu\mu+\mathrm{jets}}^{Z\to\nu\bar{\nu}}$	$\mathcal{T}_{\gamma+\mathrm{jets}}^{Z\to\nu\bar{\nu}}$
Scale factors (applied to simulation):				
Jet energy scale	< 15	< 15	< 10	< 15
b tagging eff & mistag rate	< 5	< 5	< 2	< 2
Lepton identification	2 − 5	2 − 5	2 − 5	−
Pileup	< 10	< 6	< 4	< 3
Top quark p_T	< 5	< 20	< 4	−
Closure tests:				
W/Z ratio	−	10 − 30	−	−
Z/γ ratio	−	−	−	10 − 30
W/$t\bar{t}$ composition	10 − 100	−	−	−
W polarisation	5 − 50	5 − 50	−	−
α_T / $\Delta\phi_{min}^*$	5 − 80	5 − 80	50 − 80	−

The aforementioned systematic uncertainties, resulting from variations in scale factors, are summarised in Table 3, along with representative magnitudes. Each source of uncertainty is assumed to vary with a fully correlated behaviour across the full phase space of the signal and control regions.

The second category of uncertainty is determined from sets of closure tests based on data control samples [31]. Each set uses the observed event counts in up to eight bins in H_T for each of the nine n_{jet} event categories in one of the three independent data control regions. These counts are used with the corresponding $\mathcal{T}$ factors, determined from simulation, to obtain a prediction $\mathcal{N}^{pred}(n_{jet}, H_T)$ of the observed yields $\mathcal{N}^{obs}(n_{jet}, H_T)$ in another control sample (or, in one case, n_b event category).

Each set of tests targets a specific (potential) source of bias in the simulation modelling that may introduce an n_{jet}- or H_T-dependent source of systematic bias in the $\mathcal{T}$ factors [31]. Several sets of tests are performed. The Z/γ ratio determined from simulation is tested against the same ratio measured using $Z(\to \mu\mu)$+jets events and the γ+jets sample. The W/Z ratio is also probed using the μ+jets and $\mu\mu$+jets samples, which directly tests the simulation modelling of vector boson production, as well as the modelling of $t\bar{t}$ contamination in the μ+jets sample. A further set probes the modelling of the relative composition between $W(\to \ell\nu)$+jets and $t\bar{t}$ events using μ+jets events containing exactly zero or one more b-tagged jets, which represents a larger extrapolation in relative composition than used in the search. The effects of W polarisation are probed by using μ+jets events with a positively charged muon to predict those containing a negatively charged muon. Finally, the accuracy of the modelling of the efficiencies of the α_T and $\Delta\phi_{min}^*$ requirements are estimated using the μ+jets sample.

For each set of tests, the level of closure, $(\mathcal{N}^{\mathrm{obs}} - \mathcal{N}^{\mathrm{pred}})/\mathcal{N}^{\mathrm{obs}}$, which considers only statistical uncertainties, is inspected to ensure no statistically significant biases are observed as a function of the nine n_{jet} categories or the eight H_{T} bins. In the absence of such a bias, the level of closure is recomputed by integrating over either all monojet and asymmetric n_{jet} categories, or the symmetric n_{jet} categories. The level of closure and its statistical uncertainty are combined in quadrature to determine additional contributions to the uncertainties in the $\mathcal{T}$ factors. These uncertainties are considered to be fully correlated between the monojet and asymmetric n_{jet} categories or the symmetric n_{jet} categories, and fully uncorrelated between these two regions in n_{jet} and H_{T} bins. If the closure tests use the $\mu\mu$+jets sample, the level of closure is determined by additionally integrating over pairs of adjacent H_{T} bins. These uncertainties, derived from the closure tests in data, are summarised in Table 3, along with representative magnitudes. These uncertainties are the dominant contribution to the total uncertainty in the $\mathcal{T}$ factors, due to the limited number of events in the data control regions.

As introduced in Section 5.4, templates are derived from simulation to predict the $H_{\mathrm{T}}^{\mathrm{miss}}$ distributions of the background. The uncertainties in the $\mathcal{T}$ factors are used to constrain the normalisation of the $H_{\mathrm{T}}^{\mathrm{miss}}$ templates. The uncertainties in the $H_{\mathrm{T}}^{\mathrm{miss}}$ shape are discussed below.

The accuracy to which the simulation describes the $H_{\mathrm{T}}^{\mathrm{miss}}$ distributions is evaluated with respect to data in each $(n_{\mathrm{jet}}, n_{\mathrm{b}}, H_{\mathrm{T}})$ bin in each of the μ+jets, $\mu\mu$+jets, and γ+jets data control regions. The level of agreement between data and simulation, defined in terms of the ratio of observed and expected counts (from simulation) as a function of $H_{\mathrm{T}}^{\mathrm{miss}}$, is parameterised using an orthogonal first-order polynomial, $f(x) = p_0 + p_1(\bar{x} - x)$, and described by two uncorrelated parameters, p_0 and p_1. A binned likelihood fit is performed in each $(n_{\mathrm{jet}}, n_{\mathrm{b}}, H_{\mathrm{T}})$ bin of each control region, and the best fit value p_1 and its uncertainty is used to determine the presence of biases dependent on $H_{\mathrm{T}}^{\mathrm{miss}}$. The pull of p_1 from a value of zero is defined as the best fit value over its standard deviation, considering only statistical uncertainties associated with the finite size of the data and simulated samples.

The lower bound of the final (open) bin in $H_{\mathrm{T}}^{\mathrm{miss}}$ is not more than 800 GeV and is bounded from above by the upper bound of the H_{T} bin in question. The lower bound of the final $H_{\mathrm{T}}^{\mathrm{miss}}$ bin is merged with lower bins if fewer than ten events in the data control regions are observed. If a bin in $(n_{\mathrm{jet}}, n_{\mathrm{b}}, H_{\mathrm{T}})$ contains fewer than ten events, the $H_{\mathrm{T}}^{\mathrm{miss}}$ template is not used and the background estimates are determined inclusively with respect to $H_{\mathrm{T}}^{\mathrm{miss}}$. The merging of bins is typically only relevant for event categories that satisfy $n_{\mathrm{b}} \geq 2$.

The presence of systematic biases is evaluated at a statistical level by considering the distribution of pulls obtained from each control region, which are consistent with statistical fluctuations, with no indication of trends across the full phase space of each control region. The p-values obtained from the fits are uniformly distributed.

The uncertainty in the $H_{\mathrm{T}}^{\mathrm{miss}}$ modelling is extracted under the hypothesis of no bias. This is done using the maximum likelihood (ML) values of the fit parameters to determine the statistical precision to which this hypothesis can be confirmed. The quadrature sum of the ML value and its uncertainty for p_1 from each fit is used to define alternative templates that represent $\pm 1\sigma$ variations to the nominal $H_{\mathrm{T}}^{\mathrm{miss}}$ template. These alternative templates are encoded in the likelihood function, as described in Section 7. The observed variations are compatible with the expected values obtained from studies relying only on simulated event samples. The uncertainties in the final $H_{\mathrm{T}}^{\mathrm{miss}}$ bin of the templates depend on the event category and H_{T} bin, and are typically found to be in the range $\sim$10–100%.

The effect on the $H_{\mathrm{T}}^{\mathrm{miss}}$ templates is determined under $\pm 1\sigma$ variations in the jet energy scale,

the efficiency and misidentification probability of b-quark jets, the efficiency to identify well-reconstructed, isolated leptons, the pileup reweighting, and the modelling of the top quark p_T. These effects are easily covered by the uncertainties determined from data, as described above, across the full phase space of the control regions, which mirror closely that of the signal region.

7 Results

A model of the observations in all data samples, described by a likelihood function, is used to obtain a prediction of the SM backgrounds and to test for the presence of new-physics signals if the signal region is included in the ML fit. The observation in each bin defined by the n_{jet}, n_b, H_T, and H_T^{miss} variables is modelled as a Poisson-distributed variable around the SM expectation and a potential signal contribution (assumed to be zero in the following discussion), where the SM expectation is the sum over the estimated contributions from all background processes according to the methods described in Section 6.

The nonmultijet backgrounds are related to the expected yields in the μ+jets, $\mu\mu$+jets, and γ+jets control samples via the transfer factors derived from simulation, as described in Section 5.5. Estimates of the contribution from multijet events in the signal region are determined according to the method described in Section 6.1, and are included in the likelihood function.

The systematic uncertainties summarised in Table 3 are accommodated in the likelihood function through the use of nuisance parameters, the measurements of which are assumed to follow a log-normal distribution. Alternative templates are used to describe the uncertainties in the modelling of the H_T^{miss} variable. A vertical template morphing scheme [90] is used to interpolate between the nominal and alternative H_T^{miss} templates. A nuisance parameter controls the interpolation, which is Gaussian distributed with a mean of zero and a standard deviation of one, where ± 1 corresponds to the alternative templates for a $\pm 1\sigma$ variation in the uncertainty. Each template is interpolated quadratically between $\pm 1\sigma$, and a linear extrapolation is employed beyond these bounds.

The pre-fit result of this search, which considers the observations in the control regions only, is summarised in Figs. 3–5 for, respectively, the monojet, asymmetric, and symmetric topologies. The figures also show the significance of deviations observed in data with respect to the pre-fit SM expectations, expressed in terms of the total uncertainty in the SM expectations. Figures 3–5 also summarise the pulls from the post-fit result, which is based on a ML fit to observations in the signal region as well as the control regions.

The data are well described by the background-only hypothesis. A goodness-of-fit test, based on a log likelihood ratio, is performed to quantify the degree of compatibility between the observed yields and the expectations under the background-only hypothesis. The alternative hypothesis is defined by a "saturated" model [91], for which the background expectation is set equal to the observed number of events, and provides a reference for the largest value that the likelihood can take for any model for the given data set. Hence, this reference can be used as a reasonable normalisation for the maximum observed for a more constraining model. A p-value of 0.20 is observed for the fit over the full signal region, and p-values in the range 0.04–1.00, consistent with a uniform distribution, are obtained when considering events categorised according to n_{jet}.

The covariance and correlation matrices for the pre-fit SM expectations in all bins of the signal region, defined by n_{jet}, n_b, H_T, and integrated over H_T^{miss}, are determined from 500 pseudo-experiments by sampling the pre-fit nuisance parameters under the background-only hypoth-
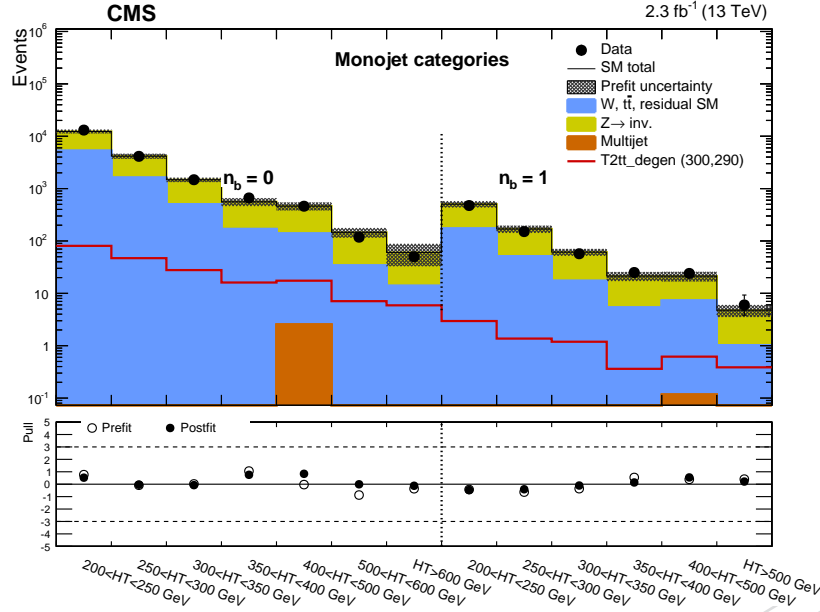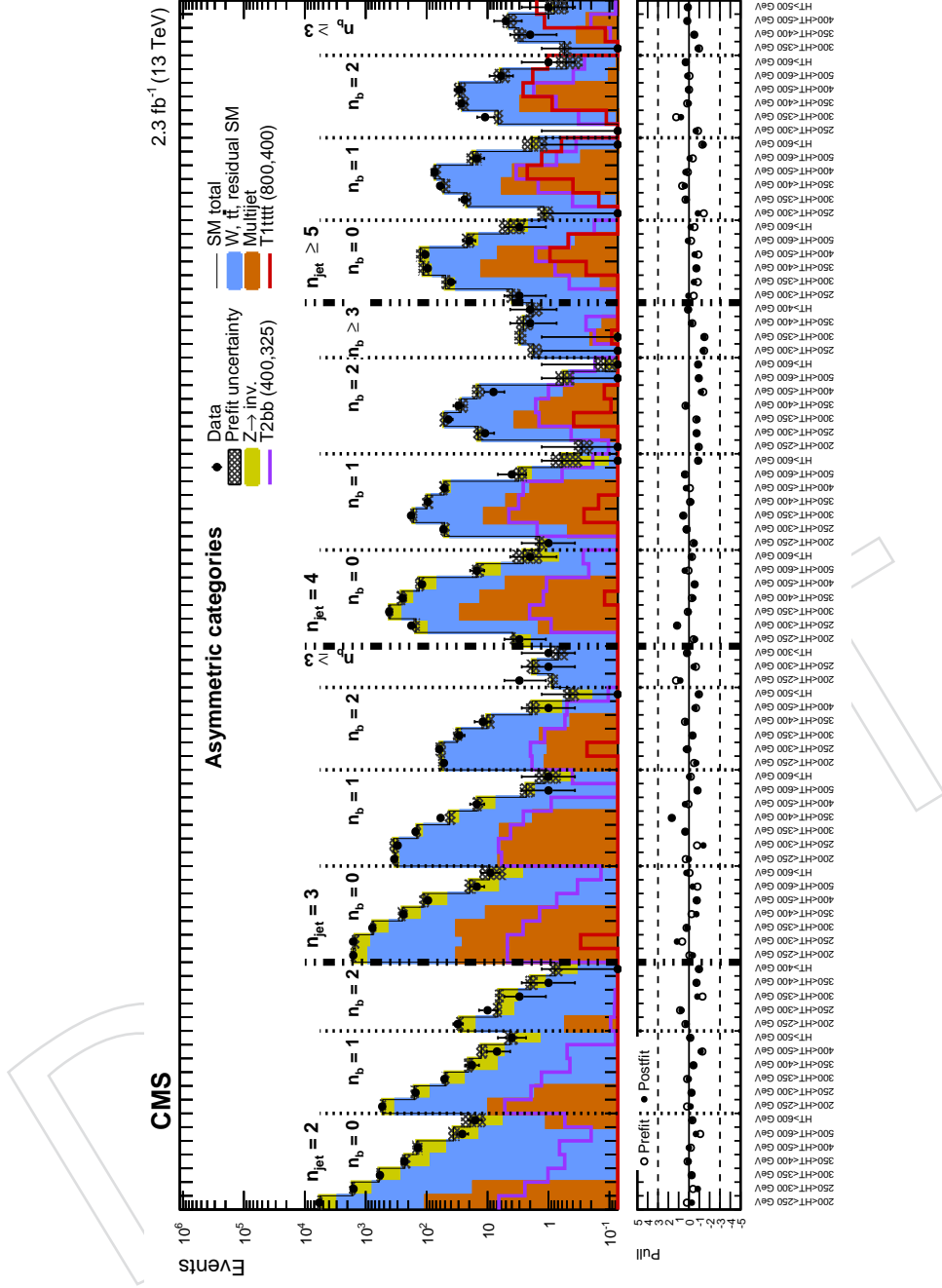
Figure 3: (Upper panel) Event yields observed in data (solid circles) and pre-fit SM expectations with their associated uncertainties (black histogram with shaded band), integrated over H_T^{miss}, as a function of n_b and H_T for the monojet category ($n_{jet} = 1$) in the signal region. For illustration only, the expectations for a benchmark model (T2tt_degen with $m_{\tilde{t}} = 300\,\text{GeV}$ and $m_{\tilde{\chi}_1^0} = 290\,\text{GeV}$) are superimposed on the SM-only expectations. (Lower panel) The significance of deviations (pulls) observed in data with respect to the pre-fit (open circles) and post-fit (closed circles) SM expectations, expressed in terms of the total uncertainty in the SM expectations. The pulls cannot be considered independently due to inter-bin correlations.

649 esis. The SM expectations for different n_{jet} and n_b categories exhibit a nonnegligible level of
650 covariance within the same H_T bin, primarily as a result of the systematic uncertainties eval-
651 uated from closure tests, described in Section 6.2, that integrate yields over n_{jet} and n_b. Bins
652 adjacent and next-to-adjacent in n_{jet} and/or n_b can have correlation coefficients in the range
653 0.2–0.4, and, infrequently, as large as ∼0.5. Otherwise, the correlation coefficients are < 0.2.
654 Anticorrelation coefficients are typically not larger than ∼0.2.

655 Figure 6 shows the event yields observed in data and pre-fit SM expectations with their asso-
656 ciated uncertainties as a function of H_T^{miss} for two categories of signal candidate events, which
657 provide good sensitivity to models with high-mass gluinos. For illustration only, the expected
658 counts from benchmark signal models that assume the pair production and decay of gluinos,
659 described further in Section 8, are also shown.

660 8 Interpretation

661 8.1 Specification for simplified models

662 The results of the search are used to constrain simplified SUSY models [92–94]. Each model
663 assumes the pair production of gluinos or squarks and their subsequent prompt decays to
664 SM particles and the LSP with a 100% branching fraction (unless indicated otherwise). The
665 gluino decays contain intermediate on-shell SUSY particle states (such as the top squark or the
666 chargino) for a subset of the models. All other SUSY particles are assumed to be too heavy
667 ($m_{\tilde{g}}/m_{\tilde{q}} = 10\,\text{TeV}$) to be produced directly. Three-body decays of gluinos are assumed to occur

Figure 4: (Upper panel) Event yields observed in data (solid circles) and pre-fit SM expectations with their associated uncertainties (black histogram with shaded band), integrated over H_T^{miss}, as a function of n_{jet}, n_b, and H_T for the asymmetric n_{jet} categories in the signal region. For illustration only, the expectations for two benchmark models (T2bb with $m_{\tilde{b}} = 400$ GeV and $m_{\tilde{\chi}_1^0} = 325$ GeV, T1tttt with $m_{\tilde{g}} = 800$ GeV and $m_{\tilde{\chi}_1^0} = 400$ GeV) are superimposed on the SM-only expectations. (Lower panel) The significance of deviations (pulls) observed in data with respect to the pre-fit (open circles) and post-fit (closed circles) SM expectations, expressed in terms of the total uncertainty in the SM expectations. The pulls cannot be considered independently due to inter-bin correlations.
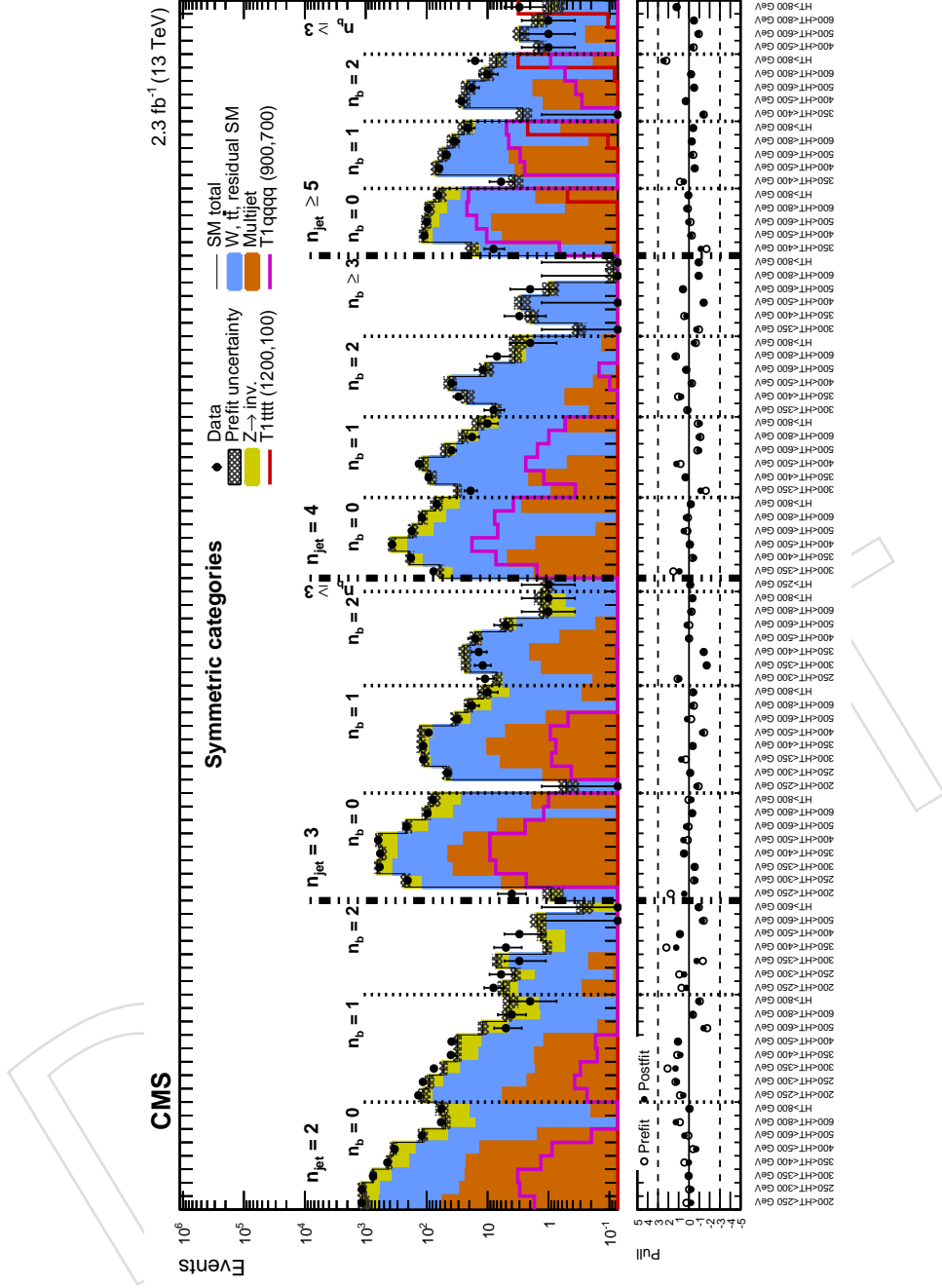
Figure 5: (Upper panel) Event yields observed in data (solid circles) and pre-fit SM expectations with their associated uncertainties (black histogram with shaded band), integrated over H_T^{miss}, as a function of n_{jet}, n_b, and H_T for the symmetric n_{jet} categories in the signal region. For illustration only, the expectations for two benchmark models (T1tttt with $m_{\tilde{g}} = 1200$ GeV and $m_{\tilde{\chi}_1^0} = 100$ GeV, T1qqqq with $m_{\tilde{g}} = 900$ GeV and $m_{\tilde{\chi}_1^0} = 700$ GeV) are superimposed on the SM-only expectations. (Lower panel) The significance of deviations (pulls) observed in data with respect to the pre-fit (open circles) and post-fit (closed circles) SM expectations, expressed in terms of the total uncertainty in the SM expectations. The pulls cannot be considered independently due to inter-bin correlations.
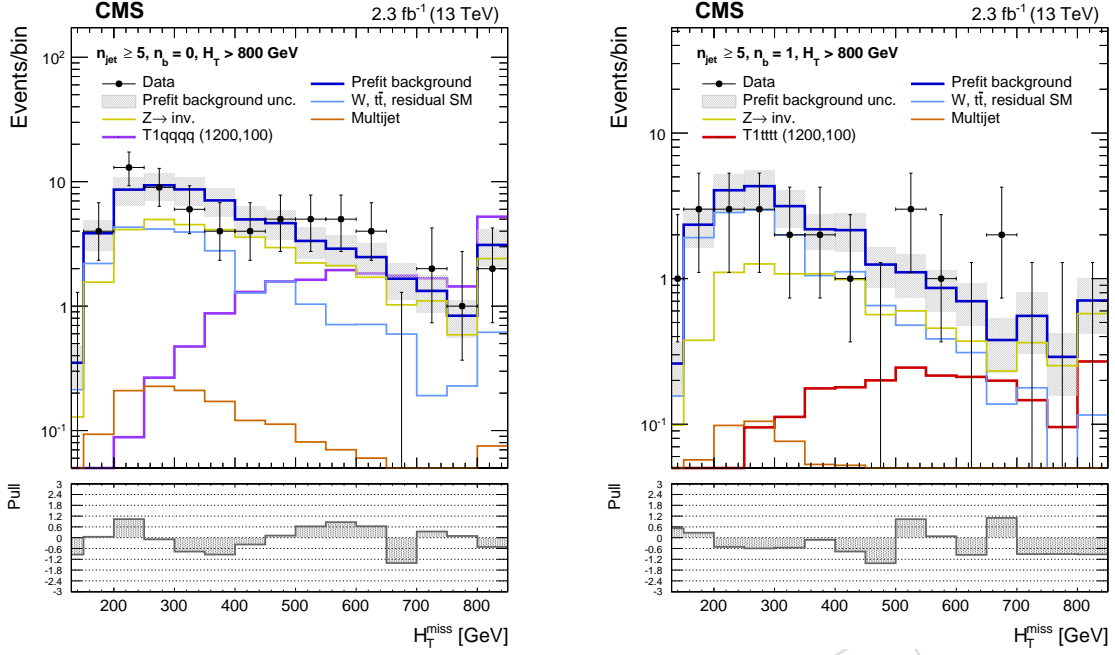
Figure 6: Event yields observed in data (solid circles) and pre-fit SM expectations with their associated uncertainties (blue histogram with shaded band) as a function of H_T^{miss} for events in the signal region that satisfy $n_{jet} \geq 5$, $H_T > 800\,\text{GeV}$, and (left) $n_b = 0$ or (right) $n_b = 1$. For illustration only, the expectations for one of two benchmark models (T1qqqq and T1tttt, both with $m_{\tilde{g}} = 1200\,\text{GeV}$ and $m_{\tilde{\chi}_1^0} = 100\,\text{GeV}$) are superimposed on the SM-only expectations. The lower panels indicate the significance of deviations (pulls) observed in data with respect to both the pre-fit SM expectations, expressed in terms of the total uncertainty in the SM expectations. The pulls cannot be considered independently due to inter-bin correlations.

668 via off-shell squarks of light or heavy flavour. Off-shell decays are processed by PYTHIA in a
669 single three- or four-body step, without taking into account the width or polarisation of the
670 parent: this is true for the top-squark four-body decay ($\tilde{t} \to bff'\tilde{\chi}_1^0$), as well as the three-body
671 decay of the chargino ($\tilde{\chi}_1^\pm \to ff'\tilde{\chi}_1^0$), where f and f' are fermions produced in the decay of an
672 intermediate off-shell W boson.

673 Fourteen unique production and decay modes are considered, which yield a range of topolo-
674 gies and final states (with only the all-jet final state considered in this search). Each class of
675 simplified model is identified by a label that indicates the topology and final state, and scans in
676 the gluino or squark ($m_{\tilde{g}}/m_{\tilde{q}}$) and LSP ($m_{\tilde{\chi}_1^0}$) mass parameter space are performed. Table 4 sum-
677 marises the production and decay modes, as well as any additional assumptions that define the
678 simplified models. The models can be categorised according to the following descriptions: the
679 gluino-mediated and direct production of light-flavour squarks, the gluino-mediated produc-
680 tion of off-shell third-generation squarks, the natural gluino-mediated production of on-shell
681 top squarks, and the direct production of on-shell third-generation squarks. In the case of direct
682 pair production of light-flavour squarks, two different assumptions on the theoretical produc-
683 tion cross section are made. For the "eightfold" scenario (T2qq_8fold), the scalar partners to
684 left- and right-handed quarks of the u, d, s, and c flavours are assumed to be light and degen-
685 erate in mass, with other squark states decoupled to a high mass. For the "onefold" scenario
686 (T2qq_1fold), only a single light squark is assumed to participate in the interaction and all
687 other squarks are decoupled to a high mass.

688 Under the signal+background hypothesis, and in the presence of a nonzero signal contribution,
689 a modified frequentist approach is used to determine upper limits at the 95% confidence level
690 (CL) on the cross section, σ_{UL}, to produce pairs of SUSY particles as a function of the parent
691 SUSY particle and the LSP masses. The limits can be expressed in terms of the signal strength
692 parameter, μ, which is determined relative to the theoretical cross section that is calculated at
693 NLO+NLL accuracy. An Asimov data set [95] is used to determine the expected upper limit on
694 the allowed cross section for a given model. The potential contributions from a new-physics
695 signal to each of the signal and control regions are considered, even though the only significant
696 contribution occurs in the signal region and not in the control regions (i.e. signal contamina-
697 tion). The approach is based on the one-sided (so called LHC-style) profile likelihood ratio
698 as the test statistic [96] and the CL_s criterion [97, 98]. Asymptotic formulae [95] are utilised
699 to approximate the distributions of the test statistics under the SM background-only and sig-
700 nal+background hypotheses.

8.2   Acceptances and uncertainties

702 The experimental acceptance times efficiency ($\mathcal{A} \times \varepsilon$) and its uncertainty are evaluated indepen-
703 dently for each model class as a function of ($m_{\mathrm{SUSY}}, m_{\mathrm{LSP}}$). Table 5 summarises $\mathcal{A} \times \varepsilon$ for a num-
704 ber of benchmark models for which the search yields an expected exclusion ($\mu \lesssim 1$). For each
705 topology, typically two different pairs of parent SUSY particle and LSP masses ($m_{\mathrm{SUSY}}, m_{\mathrm{LSP}}$)
706 are chosen that are characterised by a large and a small (i.e. compressed) difference in parent
707 SUSY particle and LSP masses. The four most sensitive event categories, defined in terms of
708 n_{jet}, are used to determine σ_{UL}. The categories used per benchmark model are listed in Table 5,
709 along with $\mathcal{A} \times \varepsilon$ determined for these four categories.

Table 4: A summary of the simplified SUSY models used to interpret the results of this search. All on-shell SUSY particles in the decay are stated.

Model class	Production	Decay	Additional assumptions
Gluino-mediated and direct production of light-flavour squarks			
T1qqqq	$pp \to \widetilde{g}\widetilde{g}$	$\widetilde{g} \to \bar{q}q\widetilde{\chi}_1^0$	–
T2qq_8fold	$pp \to \widetilde{q}\bar{\widetilde{q}}$	$\widetilde{q} \to q\widetilde{\chi}_1^0$	$m_{\widetilde{q}} = m_{\widetilde{q}_L} = m_{\widetilde{q}_R}$, $\widetilde{q} = \{\widetilde{u},\widetilde{d},\widetilde{s},\widetilde{c}\}$
T2qq_1fold	$pp \to \widetilde{q}\bar{\widetilde{q}}$	$\widetilde{q} \to q\widetilde{\chi}_1^0$	$m_{\widetilde{q}(\widetilde{q}\neq\widetilde{u}_L)} \gg m_{\widetilde{u}_L}$
Gluino-mediated production of off-shell third-generation squarks			
T1bbbb	$pp \to \widetilde{g}\widetilde{g}$	$\widetilde{g} \to \bar{b}b\widetilde{\chi}_1^0$	–
T1tttt	$pp \to \widetilde{g}\widetilde{g}$	$\widetilde{g} \to \bar{t}t^* \to \bar{t}t\widetilde{\chi}_1^0$	–
T1ttbb	$pp \to \widetilde{g}\widetilde{g}$	$\widetilde{g} \to \bar{t}b\widetilde{\chi}_1^\pm \to \bar{t}bW^*\widetilde{\chi}_1^0$	$m_{\widetilde{\chi}_1^\pm} - m_{\widetilde{\chi}_1^0} = 5\,\mathrm{GeV}$
Natural gluino-mediated production of on-shell top squarks			
T5tttt_DM175	$pp \to \widetilde{g}\widetilde{g}$	$\widetilde{g} \to \widetilde{t}\bar{t} \to \bar{t}t\widetilde{\chi}_1^0$	$m_{\widetilde{t}} - m_{\widetilde{\chi}_1^0} = 175\,\mathrm{GeV}$
T5ttcc	$pp \to \widetilde{g}\widetilde{g}$	$\widetilde{g} \to \widetilde{t}\bar{t} \to \bar{t}c\widetilde{\chi}_1^0$	$m_{\widetilde{t}} - m_{\widetilde{\chi}_1^0} = 20\,\mathrm{GeV}$
Direct production of on-shell third-generation squarks			
T2bb	$pp \to \widetilde{b}\bar{\widetilde{b}}$	$\widetilde{b} \to b\widetilde{\chi}_1^0$	–
T2tb	$pp \to \widetilde{t}\bar{\widetilde{t}}$	$\widetilde{t} \to t\widetilde{\chi}_1^0$ or $b\widetilde{\chi}_1^\pm \to bW^*\widetilde{\chi}_1^0$	50/50%, $m_{\widetilde{\chi}_1^\pm} - m_{\widetilde{\chi}_1^0} = 5\,\mathrm{GeV}$
T2tt	$pp \to \widetilde{t}\bar{\widetilde{t}}$	$\widetilde{t} \to t\widetilde{\chi}_1^0$	–
T2cc	$pp \to \widetilde{t}\bar{\widetilde{t}}$	$\widetilde{t} \to c\widetilde{\chi}_1^0$	$10 < m_{\widetilde{t}} - m_{\widetilde{\chi}_1^0} < 80\,\mathrm{GeV}$
T2tt_degen	$pp \to \widetilde{t}\bar{\widetilde{t}}$	$\widetilde{t} \to bW^*\widetilde{\chi}_1^0$	$10 < m_{\widetilde{t}} - m_{\widetilde{\chi}_1^0} < 80\,\mathrm{GeV}$
T2tt_mixed	$pp \to \widetilde{t}\bar{\widetilde{t}}$	$\widetilde{t} \to c\widetilde{\chi}_1^0$ or $bW^*\widetilde{\chi}_1^0$	50/50%, $10 < m_{\widetilde{t}} - m_{\widetilde{\chi}_1^0} < 80\,\mathrm{GeV}$

Table 5: A summary of benchmark simplified models, the most sensitive n_{jet} categories, and representative values for the corresponding experimental acceptance times efficiency ($\mathcal{A} \times \varepsilon$), the dominant systematic uncertainties, the theoretical production cross section (σ_{theory}), and the expected and observed upper limits on the production cross section, expressed in terms of the signal strength parameter (μ).

Benchmark models $(m_{\text{SUSY}}, m_{\text{LSP}})$ [GeV]		Most sensitive n_{jet} categories	$\mathcal{A} \times \varepsilon$ [%]	Systematic uncertainties [%]				σ_{theory} [fb]	μ (95% CL)	
				MC stat.	ISR	JEC	SF$_{\text{b-tag}}$		Exp.	Obs.
T1qqqq	(1300, 100)	≥5, 4, 3, 2	9.4	7-30	∼2	4-21	2-14	46.1	0.79	0.76
	(900, 700)	≥5, ≥5a, 4, 4a	5.6	10-33	1-13	1-26	1-10	677	0.58	0.44
T2qq_8fold	(1050, 100)	≥5, 3, 4, 2	17.9	7-33	1-4	3-16	1-11	35.2	0.90	0.63
	(650, 550)	≥5, 4, ≥5a, 4a	2.6	10-28	1-16	2-29	1-6	864	0.93	0.80
T2qq_1fold	(600, 50)	≥5, 3, 2, 4	13.4	5-33	1-5	1-30	1-8	177	0.78	0.84
	(400, 250)	≥5, 4, ≥5a, 3	2.9	8-30	1-8	3-25	1-7	1849	0.73	0.71
T1bbbb	(1500, 100)	≥5, 4, 3, 2	10.1	5-17	1-2	1-12	2-22	14.2	0.81	0.79
	(1000, 800)	≥5, 4, ≥5a, 4a	4.9	8-31	1-17	1-40	1-14	325	0.33	0.32
T1tttt	(1300, 100)	≥5, ≥5a, 4, 3	2.4	7-16	1-2	2-7	2-12	46.1	1.00	1.89
	(800, 400)	≥5, ≥5a, 4, 4a	0.6	7-27	1-2	3-45	1-8	1490	0.56	1.03
T1ttbb	(1300, 100)	≥5, 4, 3, ≥5a	3.8	9-32	1-2	3-16	2-19	46.1	0.60	0.91
	(1000, 700)	≥5, ≥5a, 4, 3	3.4	9-30	1-9	3-65	1-14	325	0.51	0.70
T5tttt_DM175	(800, 100)	≥5, ≥5a, 3, 4	0.2	12-20	2-4	3-5	1-6	1490	0.69	1.19
	(700, 400)	≥5, ≥5a, 4, 4a	0.2	20-29	2-10	8-10	1-2	3530	1.00	1.35
T5ttcc	(1200, 200)	≥5, 4, 3, ≥5a	4.9	6-25	5-25	3-21	1-24	85.6	0.58	0.87
	(750, 600)	≥5, ≥5a, 4, 4a	1.0	9-23	1-4	5-21	1-3	2270	0.89	0.72
T2bb	(800, 50)	2, 3, 4, ≥5	1.5	5-31	2-6	1-21	1-23	28.3	0.96	1.06
	(375, 300)	≥5, 4, 3a, 3	0.1	8-33	1-10	3-25	1-7	2610	0.67	0.87
T2tb	(600, 50)	≥5, 4, 3, 2	6.1	3-28	1-3	1-22	1-17	175	0.70	1.35
	(350, 225)	≥5, 4, 3, 3a	1.0	9-33	1-4	2-41	1-8	3790	0.79	0.88
T2tt	(700, 50)	≥5, 4, 3, ≥5a	8.1	8-33	1-4	2-22	1-21	67.0	0.90	1.19
	(350, 100)	≥5, ≥5a, 4a, 4	1.4	7-31	1-1	1-28	1-7	3790	0.44	0.50
T2cc	(325, 305)	≥5, 4, 3, 2	0.8	3-32	1-27	1-27	1-12	5600	0.92	0.68
T2tt_degen	(300, 290)	3, 4, ≥5, 2	0.9	2-27	1-27	1-25	1-12	8520	0.56	0.41
T2tt_mixed	(300, 250)	≥5, 4, ≥5a, 4a	0.4	3-33	1-27	1-33	1-13	8520	0.99	0.58

Contributions from several sources to the uncertainty in $\mathcal{A} \times \varepsilon$ are considered. Each source of uncertainty is included in the likelihood function via alternative shapes to the nominal $H_{\text{T}}^{\text{miss}}$ templates evaluated from simulated signal events categorised according to n_{jet}, n_{b}, and H_{T}. Correlations are taken into account where appropriate, including those relevant to signal contamination in the control regions. The morphing scheme that interpolates between the nominal and alternative $H_{\text{T}}^{\text{miss}}$ templates, described in Section 7, is also used for the simulated signal samples.

In addition to the uncertainty in the integrated luminosity of 2.7% [99], the following sources of uncertainty are dominant: the statistical uncertainty arising from the finite size of simulated signal samples, the modelling of ISR, the jet energy corrections (JEC) evaluated in simulation, and the modelling of scale factors applied to simulated event samples that correct for differences in the efficiency and misidentification probability of b-quark jets (SF$_{\text{b-tag}}$). The magnitude of each contribution depends on the model and the masses of the parent SUSY particle and LSP.

The $\mathcal{A} \times \varepsilon$ for models with small mass splittings (e.g. $m_{\widetilde{q}} - m_{\widetilde{\chi}_1^0} \lesssim m_{\text{t}}$) is due largely to ISR, the modelling of which is evaluated by comparing the simulated and measured p_{T} spectra of the

725 system recoiling against the ISR jets in $t\bar{t}$ events, using the technique described in Ref. [100].
726 The uncertainty can be as large as $\sim$30%, and is the dominant systematic uncertainty for sys-
727 tems with a compressed mass spectrum. Uncertainties in the jet energy scale, as large as $\sim$40%,
728 can also be dominant for models characterised by high jet multiplicities in the final state. The
729 uncertainties in $SF_{\text{b-tag}}$ can be as large as $\sim$25%. Table 5 summarises these dominant contribu-
730 tions to the uncertainty in $\mathcal{A} \times \varepsilon$ for a range of benchmark models. Characteristic values for
731 each model are expressed in terms of a range that is representative of the values across all bins
732 of the signal region. The upper bound for each range may be subject to moderate statistical
733 fluctuations.

734 Further uncertainties with subdominant contributions are considered on a similar footing. The
735 uncertainties in the efficiency of identifying well-reconstructed, isolated leptons are considered,
736 with a typical magnitude of $\sim$5% and treated as anticorrelated between the signal and control
737 regions. The uncertainty of 5% in σ_{in} is propagated through to the reweighting procedure to
738 account for differences between the simulated and measured pileup. Finally, uncertainties in
739 the simulation modelling of the efficiencies of the trigger strategy employed by the search are
740 typically $<$10%.

741 The choice of PDF set, or variations therein, predominantly affects $\mathcal{A} \times \varepsilon$ through changes in the
742 p_{T} spectrum of the system recoil, which is covered by the ISR uncertainty, hence no additional
743 uncertainty is adopted. Uncertainties in $\mathcal{A} \times \varepsilon$ due to variations in the renormalisation and
744 factorisation scales are determined to be $\sim$5%. In both cases, contributions to the uncertainty
745 in the theoretical production cross section are considered.

8.3   Cross section and mass exclusions

747 Limits for each of the aforementioned benchmark models are summarised in Table 5, expressed
748 in terms of μ. All benchmark models are expected to be excluded. The observed limits fluctuate
749 around the expected μ values, with some models exhibiting a moderately weaker than expected
750 limit.

751 Figures 7 and 8 summarise the disfavoured regions of the mass parameter space for the four-
752 teen classes of simplified models. These regions are derived by comparing the upper limits on
753 the measured fiducial cross section, corrected for the experimental $\mathcal{A} \times \varepsilon$, with the theoretical
754 cross sections calculated at NLO+NLL accuracy in α_{s} [33]. The former cross section value is
755 determined as a function of $m_{\tilde{g}}$ or $m_{\tilde{q}}$ and $m_{\tilde{\chi}_1^0}$, while the latter has a dependence solely on $m_{\tilde{g}}$
756 or $m_{\tilde{q}}$. The exclusion of models is evaluated using observed data counts in the signal region
757 (solid contours) and also expected counts based on an Asimov data set (dashed contours).

758 Figure 7 (upper) shows the excluded mass parameter space for models that assume the gluino-
759 mediated or direct production of light-flavour squarks. The excluded region extends to higher
760 masses for the gluino-mediated production of light-flavour squarks (T1qqqq), with respect to
761 direct pair production when assuming an eightfold degeneracy in mass (T2qq_8fold), due to
762 a combination of a higher gluino pair production cross section and a final state characterised
763 by higher jet multiplicities, which are exploited to provide better signal-to-background sepa-
764 ration. The excluded mass region is significantly reduced when assuming only a single light
765 squark (T2qq_1fold), with limits weakening due to the lower production cross section, com-
766 pounded by the reduced signal-to-background ratios achieved in the core of distributions in
767 the discriminating variables.

768 Figure 7 (lower) shows the exclusion contours for models that assume the gluino-mediated
769 pair production of off-shell third-generation squarks. For the topologies T1tttt and T1bbbb,
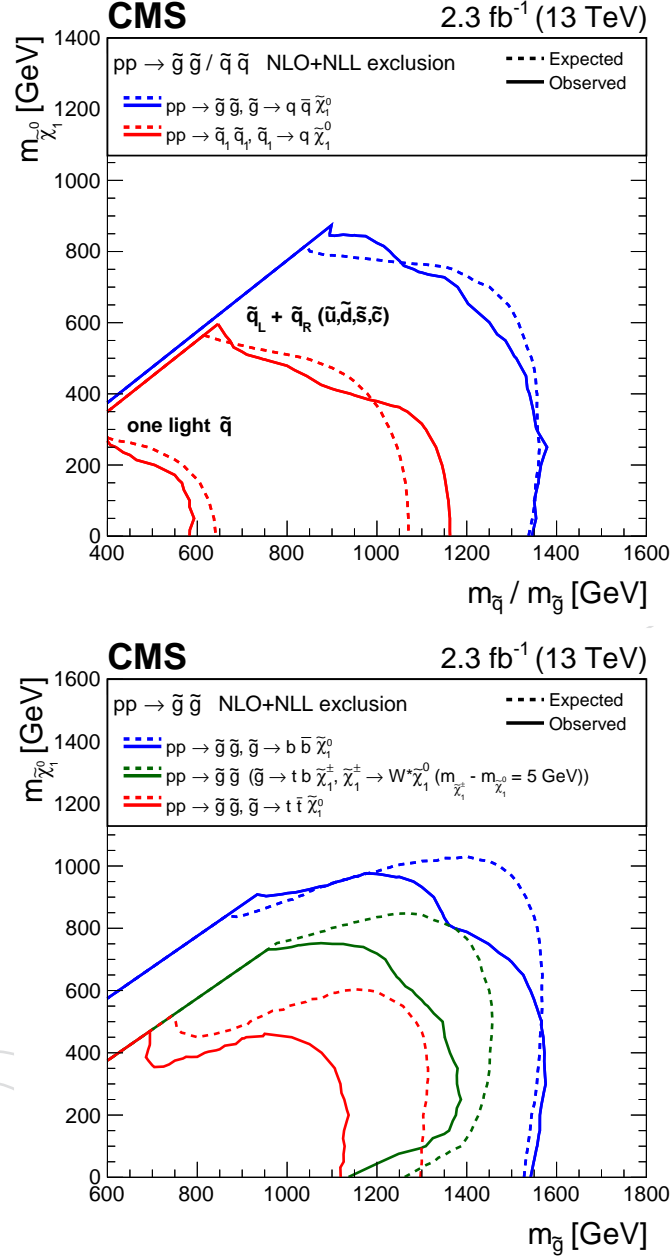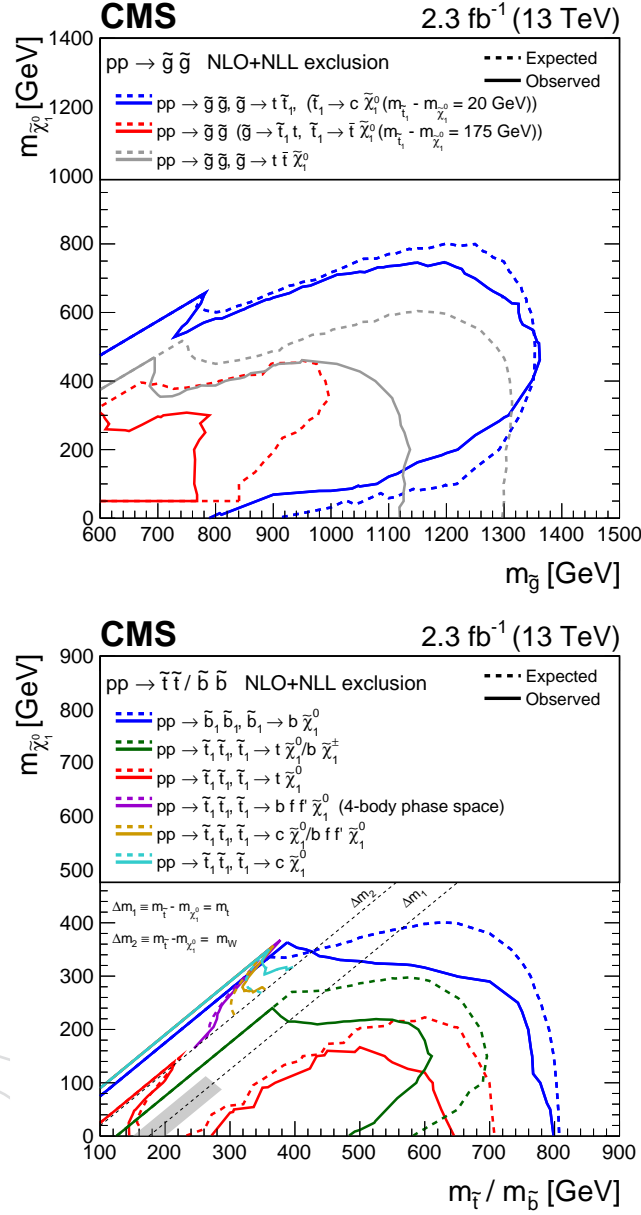
Figure 7: Observed and expected mass exclusions at 95% CL (indicated, respectively, by solid and dashed contours) for various classes of simplified models. (Upper) Gluino-mediated or direct pair production of light-flavour squarks. The two scenarios involve, respectively, the decay $\widetilde{g} \to \bar{q}q\widetilde{\chi}_1^0$ (T1qqqq) and $\widetilde{q} \to q\widetilde{\chi}_1^0$, and the latter involves two assumptions on the mass degeneracy of the squarks (T2qq_8fold and T2qq_1fold). (Lower) Three scenarios involving the gluino-mediated pair production of off-shell third-generation squarks: $\widetilde{g} \to \bar{b}b\widetilde{\chi}_1^0$ (T1bbbb), $\widetilde{g} \to \widetilde{t}\widetilde{t}^* \to \bar{t}t\widetilde{\chi}_1^0$ (T1tttt), and $\widetilde{g} \to \bar{t}b\widetilde{\chi}_1^{\pm} \to \bar{t}bW^*\widetilde{\chi}_1^0$ (T1ttbb).

Figure 8: Observed and expected mass exclusions at 95% CL (indicated, respectively, by solid and dashed contours) for a number of simplified models. (Upper) Two scenarios involving the gluino-mediated pair production of on-shell top squarks: $\widetilde{g} \to \overline{t}t \to \overline{t}t\widetilde{\chi}_1^0$ with $m_{\widetilde{t}} - m_{\widetilde{\chi}_1^0} = 175\,\text{GeV}$ (T5tttt_DM175) and $\widetilde{g} \to \overline{t}t \to \overline{t}c\widetilde{\chi}_1^0$ with $m_{\widetilde{t}} - m_{\widetilde{\chi}_1^0} = 20\,\text{GeV}$ (T5ttcc). Also shown, for comparison, is T1tttt. (Lower) Six scenarios involving the direct pair production of third-generation squarks. The first scenario involves the pair production of bottom squarks, $\widetilde{b} \to b\widetilde{\chi}_1^0$ (T2bb). Two scenarios involve the decay of top squark pairs as follows: $\widetilde{t} \to t\widetilde{\chi}_1^0$ or $\widetilde{t} \to b\widetilde{\chi}_1^\pm \to bW^*\widetilde{\chi}_1^0$ with $m_{\widetilde{\chi}_1^\pm} - m_{\widetilde{\chi}_1^0} = 5\,\text{GeV}$ and branching fractions 50/50% (T2tb), or $\widetilde{t} \to t\widetilde{\chi}_1^0$ (T2tt). The final three scenarios consider top squark decays under the assumption $10 < m_{\widetilde{t}} - m_{\widetilde{\chi}_1^0} < 80\,\text{GeV}$: $\widetilde{t} \to c\widetilde{\chi}_1^0$ (T2cc), $\widetilde{t} \to bW^*\widetilde{\chi}_1^0$ (T2tt_degen), and $\widetilde{t} \to c\widetilde{\chi}_1^0$ or $\widetilde{t} \to bW^*\widetilde{\chi}_1^0$ with branching fractions 50/50% (T2tt_mixed). The grey shaded region denotes T2tt models that are not considered for interpretation.

each gluino is assumed to undergo a three-body decay via, respectively, an off-shell top or bottom squark to a quark-antiquark pair of the same flavour and the $\widetilde{\chi}_1^0$. In the case of `T1ttbb`, each gluino is assumed to undergo a three-body decay to an on-shell chargino, $\widetilde{\chi}_1^\pm$, a bottom quark, and a top antiquark. The chargino mass is defined relative to the neutralino mass via the expression $m_{\widetilde{\chi}_1^\pm} - m_{\widetilde{\chi}_1^0} = 5\,\text{GeV}$. The chargino decays promptly to the $\widetilde{\chi}_1^0$ and an off-shell W boson. The excluded mass regions differ significantly for these topologies, primarily due to the different number of (on-shell) W bosons in their final states, resulting in the highest $\mathcal{A} \times \varepsilon$ for `T1bbbb` and lowest for `T1tttt`. Further, $\mathcal{A} \times \varepsilon$ has a strong dependence on jet multiplicity, which is highest for `T1tttt`, due to the $\Delta\phi^*_{\min}$ variable. An additional feature for `T1ttbb` is the weakening of the mass limit at low values of $m_{\widetilde{\chi}_1^0}$, when $m_{\widetilde{\chi}_1^\pm} = m_{\widetilde{\chi}_1^0} + 5\,\text{GeV} \lesssim m_t$. In this scenario, the $\widetilde{\chi}_1^\pm$ (and hence $\widetilde{\chi}_1^0$) is not highly Lorentz boosted relative to the top quark resulting from the three-body decay of the gluino. Hence, two $\widetilde{\chi}_1^0$ SUSY particles do not carry away significant $\vec{p}_T^{\text{miss}}$, which is instead realised through W boson decays to neutrinos and "lost" leptons or τ leptons that decay to neutrinos and hadrons. The observed mass limits for these topologies are up to $\sim$2 standard deviations weaker than the expected limits. These differences are due to upward fluctuations in data for two contiguous bins that satisfy the requirements $n_{\text{jet}} \geq 5$, $n_{\text{b}} \geq 2$, and $H_T > 800\,\text{GeV}$. This region has the highest sensitivity to models involving gluino production and decays to third-generation quarks (via on- or off-shell squarks). The observed counts are consistent with statistical fluctuations and the events do not exhibit anomalous nonphysical behaviour. The events are distributed in H_T^{miss} consistent with expectation, hence models characterised by high values of H_T^{miss}, such as `T1bbbb` with $m_{\widetilde{g}} \gg m_{\widetilde{\chi}_1^0}$ or $m_{\widetilde{g}} \approx m_{\widetilde{\chi}_1^0}$, are less compatible with the data counts in this high-n_{jet}, n_{b}, and H_T region.

Figure 8 (upper) shows exclusion contours for models that assume gluino pair production, with each gluino decaying to a top quark and an on-shell top squark, the latter of which decays to SM particles and the LSP. As discussed earlier, these models can be considered as representations of a natural solution to the little hierarchy problem. Two different scenarios are considered for the decay of the top squarks. The `T5tttt_DM175` models assume a two-body decay to a top quark and the $\widetilde{\chi}_1^0$, with the top squark mass defined relative to the $\widetilde{\chi}_1^0$ as $m_{\widetilde{t}} - m_{\widetilde{\chi}_1^0} = m_t$. Models that satisfy $m_{\widetilde{\chi}_1^0} < 50\,\text{GeV}$ are not considered here, as the $\widetilde{\chi}_1^0$ particles carry very little momentum. The `T5ttcc` models assume $m_{\widetilde{t}} - m_{\widetilde{\chi}_1^0} = 20\,\text{GeV}$ and two-body decays to a charm quark and the $\widetilde{\chi}_1^0$.

Finally, Fig. 8 (lower) shows exclusion contours for models that assume the direct production of pairs of third-generation squarks. For the `T2bb` models, bottom squarks are pair produced and each decays to a bottom quark and the $\widetilde{\chi}_1^0$. The `T2tt` models assume top squarks are pair produced and each is assumed to undergo a two- or three-body decay to, respectively, a top quark and the $\widetilde{\chi}_1^0$ when $m_{\widetilde{t}} - m_{\widetilde{\chi}_1^0} > m_t$ is satisfied, or a b quark, an on-shell W boson, and the $\widetilde{\chi}_1^0$ for the condition $m_W < m_{\widetilde{t}} - m_{\widetilde{\chi}_1^0} < m_t$. Models that satisfy $|m_{\widetilde{t}} - m_t - m_{\widetilde{\chi}_1^0}| < 25\,\text{GeV}$ and $m_{\widetilde{t}} + m_{\widetilde{\chi}_1^0} < 375\,\text{GeV}$ are not considered here, as σ_{UL} is a strong function of $m_{\widetilde{t}} - m_{\widetilde{\chi}_1^0}$ in this low-$m_{\widetilde{t}}$ region due to the high levels of signal contamination found in the μ+jets control region for models that resemble the $t\bar{t}$ background in terms of their topological and kinematic properties. The `T2tb` models also assume the pair production of top squarks, with each undergoing a two-body decay to either a top quark and the $\widetilde{\chi}_1^0$, or a bottom quark and the $\widetilde{\chi}_1^\pm$, with equal branching fractions of 50%. As for the `T1ttbb` models, the chargino mass is defined relative to the neutralino mass via the expression $m_{\widetilde{\chi}_1^\pm} - m_{\widetilde{\chi}_1^0} = 5\,\text{GeV}$, and the chargino decays promptly to the $\widetilde{\chi}_1^0$ and an off-shell W boson. The excluded mass regions differ significantly for the `T2bb`, `T2tb`, and `T2tt` topologies, in an analogous way to the `T1bbbb`, `T1ttbb`, and `T1tttt` models

Table 6: Summary of the mass limits obtained for the fourteen classes of simplified models. The limits indicate the strongest observed and expected (in parentheses) mass exclusions in $\widetilde{g}$, $\widetilde{q}$, $\widetilde{b}$, $\widetilde{t}$, and $\widetilde{\chi}_1^0$. The quoted values have uncertainties of ± 25 and ± 10 GeV for models involving the pair production of, respectively, gluinos and squarks.

Model class	Parent SUSY particle	Best mass limit [GeV]	
		$\widetilde{g}/\widetilde{q}/\widetilde{b}/\widetilde{t}$	$\widetilde{\chi}_1^0$
T1qqqq	$\widetilde{g}$	1375 (1350)	875 (850)
T2qq_8fold	$\widetilde{q}$	1150 (1075)	600 (550)
T2qq_1fold	$\widetilde{q}$	575 (650)	275 (275)
T1bbbb	$\widetilde{g}$	1575 (1575)	975 (1025)
T1tttt	$\widetilde{g}$	1125 (1325)	475 (600)
T1ttbb	$\widetilde{g}$	1375 (1450)	750 (850)
T5tttt_DM175	$\widetilde{g}$	800 (1000)	300 (450)
T5ttcc	$\widetilde{g}$	1350 (1350)	700 (800)
T2bb	$\widetilde{b}$	800 (800)	360 (400)
T2tb	$\widetilde{t}$	610 (690)	240 (300)
T2tt (3-body)	$\widetilde{t}$	670 (720)	210 (240)
T2tt (2-body)	$\widetilde{t}$	280 (280)	200 (200)
T2cc	$\widetilde{t}$	400 (350)	310 (340)
T2tt_degen	$\widetilde{t}$	370 (360)	360 (350)
T2tt_mixed	$\widetilde{t}$	360 (350)	350 (340)

817 described above. The difference in the mass exclusions is due primarily to the different number
818 of (on-shell) W bosons in the final states, which affects $\mathcal{A} \times \varepsilon$ through the presence of leptons
819 from the decay of the W boson. An additional feature for T2tb is the weakening of the mass
820 limit at low values of $m_{\widetilde{\chi}_1^0}$, when $m_{\widetilde{\chi}_1^\pm} = m_{\widetilde{\chi}_1^0} + 5 \, \text{GeV} \lesssim m_t$. Moderately weaker than expected
821 mass limits are observed for all models involving two-body decays, which is traced to mild
822 upward fluctuations in data for events satisfying $n_{\text{jet}} = 2$, $n_b = 2$, and $350 < H_T < 500 \, \text{GeV}$.

823 Figure 8 (lower) also shows exclusion contours for models that assume the pair production of
824 top squarks but a near-mass-degenerate system that satisfies $10 \, \text{GeV} < m_{\widetilde{t}} - m_{\widetilde{\chi}_1^0} < m_W$. Two
825 decays of the top squark are considered. The T2cc and T2tt_degen models assume two- and
826 four-body decays of the top squark to, respectively, a charm quark and the $\widetilde{\chi}_1^0$, or to $bf\bar{f}'\widetilde{\chi}_1^0$,
827 where f and $\bar{f}'$ are fermions produced in the decay of an intermediate off-shell W boson. A
828 third class of models, T2tt_mixed, assumes both these decay modes with an equal branching
829 fraction of 50%. For T2cc, the excluded mass region is relatively stable as a function of the
830 mass splitting $\Delta m = m_{\widetilde{t}} - m_{\widetilde{\chi}_1^0}$, with $\widetilde{t}$ masses excluded up to 400 GeV. For T2tt_degen, the
831 excluded mass region is strongly dependent on Δm, weakening considerably for increasing
832 values of Δm due to the increased momentum phase space available to leptons produced in the
833 four-body decay. The T2tt_mixed models exhibit an intermediate behaviour. Mass limits for
834 all three model classes converge for the smallest mass splitting considered, $\Delta m = 10 \, \text{GeV}$, when
835 the SM particles from the $\widetilde{t}$ decay are extremely soft and outside the experimental acceptance.
836 An approximately contiguous mass exclusion limit is observed across the transition from the
837 T2tt_degen four-body to the T2tt three-body decay of the $\widetilde{t}$, as the top quark moves on-shell.
838 The excluded mass region weakens further as $\Delta m \to m_t$.

839 Table 6 summarises the strongest expected and observed excluded $m_{\widetilde{g}}$ or $m_{\widetilde{q}}$ and $m_{\widetilde{\chi}_1^0}$ masses
840 for each class of simplified model.

9 Summary

An inclusive search for new-physics phenomena is reported, based on data from pp collisions at $\sqrt{s} = 13$ TeV. The data are recorded with the CMS detector and correspond to an integrated luminosity of 2.3 ± 0.1 fb^{-1}. The final states analysed contain one or more jets with large transverse momenta and a significant imbalance of transverse momentum, as expected from the production of massive coloured SUSY particles, each decaying to SM particles and the lightest stable, weakly-interacting, SUSY particle.

The sums of the standard model backgrounds are estimated from a simultaneous binned likelihood fit to the observed yields for samples of events categorised according to the number of reconstructed jets, the number of jets identified as originating from b quarks, and the scalar and the magnitude of the vector sums of the transverse momenta of jets. In addition to the signal region, μ+jets, $\mu\mu$+jets, and γ+jets control regions are included in the likelihood fit. The observed yields are found to be in agreement with the expected contributions from standard model processes. The search result is interpreted in the mass parameter space of fourteen simplified SUSY models, which cover scenarios that involve the gluino-mediated or direct production of light- or heavy-flavour squarks, intermediate SUSY particle states, as well as natural and nearly mass-degenerate spectra.

The increase in the centre-of-mass energy of the LHC, from 8 to 13 TeV, provides a significant gain in sensitivity to heavy particle states such as gluinos. In the case of pair-produced gluinos, each decaying via an off-shell b squark to the b quark and the LSP, models with masses up to $\sim$1.6 and $\sim$1.0 TeV are excluded for, respectively, the gluino and LSP. These limits improve on those obtained at $\sqrt{s} = 8$ TeV by, respectively, $\sim$250 and $\sim$300 GeV. In the case of direct pair production, models with masses up to $\sim$800 and $\sim$350 GeV are excluded for, respectively, the b squark and LSP. These mass limits are sensitive to the assumptions on the squark flavour and the presence of intermediate states such as charginos.

Finally, a comprehensive study of nearly mass-degenerate models involving top squark pair production is performed. The two decay modes of the top squark are the loop-induced two-body decay to the neutralino and one c quark, and the four-body decay to the neutralino, one b quark, and an off-shell W boson. A third scenario is considered in which the two modes are simultaneously open, each with a branching fraction of 50%. Masses of the top squark and LSP up to, respectively, 400 and 360 GeV are excluded, depending on the decay modes considered.

In conclusion, the analysis provides sensitivity across a large region of the natural SUSY parameter space, as characterised by interpretations with several simplified models. In particular, these studies improve on existing limits for nearly mass-degenerate models involving the production of pairs of top squarks.

Acknowledgments

References

[1] Y. A. Gol'fand and E. P. Likhtman, "Extension of the Algebra of Poincaré Group Generators and Violation of p Invariance", *JETP Lett.* **13** (1971) 323.

[2] J. Wess and B. Zumino, "Supergauge transformations in four dimensions", *Nucl. Phys. B* **70** (1974) 39, doi:10.1016/0550-3213(74)90355-1.

[3] R. Barbieri, S. Ferrara, and C. A. Savoy, "Gauge Models with Spontaneously Broken Local Supersymmetry", *Phys. Lett. B* **119** (1982) 343, doi:10.1016/0370-2693(82)90685-2.

[4] H. P. Nilles, "Supersymmetry, Supergravity and Particle Physics", *Phys. Rept.* **110** (1984) 1, doi:10.1016/0370-1573(84)90008-5.

[5] S. Dawson, E. Eichten, and C. Quigg, "Search for Supersymmetric Particles in Hadron–Hadron Collisions", *Phys. Rev. D* **31** (1985) 1581, doi:10.1103/PhysRevD.31.1581.

[6] H. Haber and G. Kane, "The Search for Supersymmetry: Probing Physics Beyond the Standard Model", *Phys. Rept.* **117** (1987) 75, doi:10.1016/0370-1573(85)90051-1.

[7] G. R. Farrar and P. Fayet, "Phenomenology of the Production, Decay, and Detection of New Hadronic States Associated with Supersymmetry", *Phys. Lett. B* **76** (1978) 575, doi:10.1016/0370-2693(78)90858-4.

[8] G. Jungman, M. Kamionkowski, and K. Griest, "Supersymmetric dark matter", *Phys. Rept.* **267** (1996) 195, doi:10.1016/0370-1573(95)00058-5, arXiv:hep-ph/9506380.

[9] Particle Data Group, "Review of Particle Physics", *Chin. Phys. C* **38** (2014) 090001.

[10] S. Dimopoulos, S. Raby, and F. Wilczek, "Supersymmetry and the Scale of Unification", *Phys. Rev. D* **24** (1981) 1681, doi:10.1103/PhysRevD.24.1681.

[11] L. E. Ibanez and G. G. Ross, "Low-Energy Predictions in Supersymmetric Grand Unified Theories", *Phys. Lett. B* **105** (1981) 439, doi:10.1016/0370-2693(81)91200-4.

[12] W. J. Marciano and G. Senjanovic, "Predictions of Supersymmetric Grand Unified Theories", *Phys. Rev. D* **25** (1982) 3092, doi:10.1103/PhysRevD.25.3092.

[13] ATLAS Collaboration, "Observation of a new particle in the search for the Standard Model Higgs boson with the ATLAS detector at the LHC", *Phys. Lett. B* **716** (2012) 1, doi:10.1016/j.physletb.2012.08.020, arXiv:1207.7214.

[14] CMS Collaboration, "Observation of a new boson at a mass of 125 GeV with the CMS experiment at the LHC", *Phys. Lett. B* **716** (2012) 30, doi:10.1016/j.physletb.2012.08.021, arXiv:1207.7235.

[15] CMS Collaboration, "Observation of a new boson with mass near 125 GeV in pp collisions at $\sqrt{s} = 7$ and 8 TeV", *JHEP* **06** (2013) 081, doi:10.1007/JHEP06(2013)081, arXiv:1303.4571.

[16] E. Witten, "Dynamical Breaking of Supersymmetry", *Nucl. Phys. B* **188** (1981) 513, doi:10.1016/0550-3213(81)90006-7.

[17] S. Dimopoulos and H. Georgi, "Softly Broken Supersymmetry and SU(5)", *Nucl. Phys. B* **193** (1981) 150, doi:10.1016/0550-3213(81)90522-8.

[18] R. Barbieri and D. Pappadopulo, "S-particles at their naturalness limits", *JHEP* **10** (2009) 061, doi:10.1088/1126-6708/2009/10/061, arXiv:0906.4546.

[19] A. Delgado et al., "The light stop window", *Eur. Phys. J. C* **73** (2013) 2370, doi:10.1140/epjc/s10052-013-2370-5, arXiv:1212.6847.

[20] C. Boehm, A. Djouadi, and Y. Mambrini, "Decays of the lightest top squark", *Phys. Rev. D* **61** (2000) 095006, doi:10.1103/PhysRevD.61.095006, arXiv:hep-ph/9907428.

[21] M. Carena, A. Freitas, and C. Wagner, "Light Stop Searches at the LHC in Events with One Hard Photon or Jet and Missing Energy", *JHEP* **10** (2008) 109, doi:10.1088/1126-6708/2008/10/109, arXiv:0808.2298.

[22] R. Grober, M. M. Muhlleitner, E. Popenda, and A. Wlotzka, "Light Stop Decays: Implications for LHC Searches", *Eur. Phys. J. C* **75** (2015) 420, doi:10.1140/epjc/s10052-015-3626-z, arXiv:1408.4662.

[23] R. Grober, M. Muhlleitner, E. Popenda, and A. Wlotzka, "Light stop decays into $Wb\widetilde{\chi}_1^0$ near the kinematic threshold", *Phys. Lett. B* **747** (2015) 144, doi:10.1016/j.physletb.2015.05.060, arXiv:1502.05935.

[24] C. Boehm, A. Djouadi, and M. Drees, "Light scalar top quarks and supersymmetric dark matter", *Phys. Rev. D* **62** (2000) 035012, doi:10.1103/PhysRevD.62.035012, arXiv:hep-ph/9911496.

[25] C. Balazs, M. S. Carena, and C. Wagner, "Dark matter, light stops and electroweak baryogenesis", *Phys. Rev. D* **70** (2004) 015007, doi:10.1103/PhysRevD.70.015007, arXiv:hep-ph/0403224.

[26] S. P. Martin, "Compressed supersymmetry and natural neutralino dark matter from top squark-mediated annihilation to top quarks", *Phys. Rev. D* **75** (2007) 115005, doi:10.1103/PhysRevD.75.115005, arXiv:hep-ph/0703097.

[27] S. P. Martin, "Top squark-mediated annihilation scenario and direct detection of dark matter in compressed supersymmetry", *Phys. Rev. D* **76** (2007) 095005, doi:10.1103/PhysRevD.76.095005, arXiv:0707.2812.

[28] CMS Collaboration, "Search for Supersymmetry in pp Collisions at 7 TeV in Events with Jets and Missing Transverse Energy", *Phys. Lett. B* **698** (2011) 196, doi:10.1016/j.physletb.2011.03.021, arXiv:1101.1628.

[29] CMS Collaboration, "Search for Supersymmetry at the LHC in Events with Jets and Missing Transverse Energy", *Phys. Rev. Lett.* **107** (2011) 221804, doi:10.1103/PhysRevLett.107.221804, arXiv:1109.2352.

[30] CMS Collaboration, "Search for supersymmetery in final states with missing transverse energy and 0, 1, 2, or $\geq$3 b-quark jets in 7 TeV pp collisions using the α_T variable", *JHEP* **01** (2013) 077, `doi:10.1007/JHEP01(2013)077`, `arXiv:1210.8115`.

[31] CMS Collaboration, "Search for supersymmetry in hadronic final states with missing transverse energy using the variables α_T and b-quark multiplicity in pp collisions at $\sqrt{s} = 8$ TeV", *Eur. Phys. J. C* **73** (2013) 2568, `doi:10.1140/epjc/s10052-013-2568-6`, `arXiv:1303.2985`.

[32] CMS Collaboration, "Search for top squark pair production in compressed-mass-spectrum scenarios in proton-proton collisions at $\sqrt{s} = 8$ TeV using the α_T variable", (2016). `arXiv:1605.08983`. Submitted to *Phys. Lett. B*.

[33] C. Borschensky et al., "Squark and gluino production cross sections in pp collisions at $\sqrt{s} = 13, 14, 33$ and 100 TeV", *Eur. Phys. J. C* **74** (2014) 3174, `doi:10.1140/epjc/s10052-014-3174-y`, `arXiv:1407.5066`.

[34] ATLAS Collaboration, "Summary of the searches for squarks and gluinos using $\sqrt{s} = 8$ TeV pp collisions with the ATLAS experiment at the LHC", *JHEP* **10** (2015) 054, `doi:10.1007/JHEP10(2015)054`, `arXiv:1507.05525`.

[35] ATLAS Collaboration, "ATLAS Run 1 searches for direct pair production of third-generation squarks at the Large Hadron Collider", *Eur. Phys. J. C* **75** (2015) 510, `doi:10.1140/epjc/s10052-015-3726-9`, `arXiv:1506.08616`. [Erratum: *Eur. Phys. J. C* **76**, (2016) 153].

[36] CMS Collaboration, "Searches for supersymmetry based on events with b jets and four W bosons in pp collisions at 8 TeV", *Phys. Lett. B* **745** (2015) 5, `doi:10.1016/j.physletb.2015.04.002`, `arXiv:1412.4109`.

[37] CMS Collaboration, "Searches for Supersymmetry using the M_{T2} Variable in Hadronic Events Produced in pp Collisions at 8 TeV", *JHEP* **05** (2015) 078, `doi:10.1007/JHEP05(2015)078`, `arXiv:1502.04358`.

[38] CMS Collaboration, "Search for direct pair production of supersymmetric top quarks decaying to all-hadronic final states in pp collisions at $\sqrt{s} = 8$ TeV", *Eur. Phys. J. C* **76** (2016) 460, `doi:10.1140/epjc/s10052-016-4292-5`, `arXiv:1603.00765`.

[39] CMS Collaboration, "Search for gluino mediated bottom- and top-squark production in multijet final states in pp collisions at 8 TeV", *Phys. Lett. B* **725** (2013) 243, `doi:10.1016/j.physletb.2013.06.058`, `arXiv:1305.2390`.

[40] CMS Collaboration, "Search for new physics in the multijet and missing transverse momentum final state in proton-proton collisions at $\sqrt{s} = 8$ TeV", *JHEP* **06** (2014) 055, `doi:10.1007/JHEP06(2014)055`, `arXiv:1402.4770`.

[41] CMS Collaboration, "Search for supersymmetry using razor variables in events with b-tagged jets in pp collisions at $\sqrt{s} = 8$ TeV", *Phys. Rev. D* **91** (2015) 052018, `doi:10.1103/PhysRevD.91.052018`, `arXiv:1502.00300`.

[42] CMS Collaboration, "Searches for third-generation squark production in fully hadronic final states in proton-proton collisions at $\sqrt{s} = 8$ TeV", *JHEP* **06** (2015) 116, `doi:10.1007/JHEP06(2015)116`, `arXiv:1503.08037`.

[43] CMS Collaboration, "Search for supersymmetry in pp collisions at $\sqrt{s} = 8$ TeV in final states with boosted W bosons and b jets using razor variables", *Phys. Rev. D* **93** (2016) 092009, `doi:10.1103/PhysRevD.93.092009`, `arXiv:1602.02917`.

[44] ATLAS Collaboration, "Search for new phenomena in final states with large jet multiplicities and missing transverse momentum with ATLAS using $\sqrt{s} = 13$ TeV proton–proton collisions", *Phys. Lett. B* **757** (2016) 334, `doi:10.1016/j.physletb.2016.04.005`, `arXiv:1602.06194`.

[45] ATLAS Collaboration, "Search for new phenomena in final states with an energetic jet and large missing transverse momentum in pp collisions at $\sqrt{s} = 13$ TeV using the ATLAS detector", (2016). `arXiv:1604.07773`. Submitted to *Phys. Rev. D*.

[46] ATLAS Collaboration, "Search for squarks and gluinos in final states with jets and missing transverse momentum at $\sqrt{s} = 13$ TeV with the ATLAS detector", *Eur. Phys. J. C* **76** (2016) 392, `doi:10.1140/epjc/s10052-016-4184-8`, `arXiv:1605.03814`.

[47] ATLAS Collaboration, "Search for pair production of gluinos decaying via stop and sbottom in events with *b*-jets and large missing transverse momentum in pp collisions at $\sqrt{s} = 13$ TeV with the ATLAS detector", *Phys. Rev. D* **94** (2016) 032003, `doi:10.1103/PhysRevD.94.032003`, `arXiv:1605.09318`.

[48] ATLAS Collaboration, "Search for bottom squark pair production in proton–proton collisions at $\sqrt{s} = 13$ TeV with the ATLAS detector", (2016). `arXiv:1606.08772`. Submitted to *Eur. Phys. J. C*.

[49] CMS Collaboration, "Search for supersymmetry in the multijet and missing transverse momentum final state in pp collisions at 13 TeV", *Phys. Lett. B* **758** (2016) 152, `doi:10.1016/j.physletb.2016.05.002`, `arXiv:1602.06581`.

[50] CMS Collaboration, "Search for new physics with the M_{T2} variable in all-jets final states produced in pp collisions at $\sqrt{s} = 13$ TeV", (2016). `arXiv:1603.04053`. Submitted to *JHEP*.

[51] P. J. Fox, R. Harnik, R. Primulando, and C.-T. Yu, "Taking a Razor to Dark Matter Parameter Space at the LHC", *Phys. Rev. D* **86** (2012) 015010, `doi:10.1103/PhysRevD.86.015010`, `arXiv:1203.1662`.

[52] O. Buchmueller, S. A. Malik, C. McCabe, and B. Penning, "Constraining Dark Matter Interactions with Pseudoscalar and Scalar Mediators using Collider Searches for Multijets plus Missing Transverse Energy", *Phys. Rev. Lett.* **115** (2015) 181802, `doi:10.1103/PhysRevLett.115.181802`, `arXiv:1505.07826`.

[53] L. Randall and D. Tucker-Smith, "Dijet Searches for Supersymmetry at the Large Hadron Collider", *Phys. Rev. Lett.* **101** (2008) 221803, `doi:10.1103/PhysRevLett.101.221803`, `arXiv:0806.1049`.

[54] CMS Collaboration, "The CMS experiment at the CERN LHC", *JINST* **3** (2008) S08004, `doi:10.1088/1748-0221/3/08/S08004`.

[55] J. Alwall et al., "The automated computation of tree-level and next-to-leading order differential cross sections, and their matching to parton shower simulations", *JHEP* **07** (2014) 079, `doi:10.1007/JHEP07(2014)079`, `arXiv:1405.0301`.

[56] S. Alioli, P. Nason, C. Oleari, and E. Re, "A general framework for implementing NLO calculations in shower Monte Carlo programs: the POWHEG BOX", *JHEP* **06** (2010) 043, doi:10.1007/JHEP06(2010)043, arXiv:1002.2581.

[57] E. Re, "Single-top Wt-channel production matched with parton showers using the POWHEG method", *Eur. Phys. J. C* **71** (2011) 1547, doi:10.1140/epjc/s10052-011-1547-z, arXiv:1009.2450.

[58] R. Gavin, Y. Li, F. Petriello, and S. Quackenbush, "W Physics at the LHC with FEWZ 2.1", *Comput. Phys. Commun.* **184** (2013) 208, doi:10.1016/j.cpc.2012.09.005, arXiv:1201.5896.

[59] R. Gavin, Y. Li, F. Petriello, and S. Quackenbush, "FEWZ 2.0: A code for hadronic Z production at next-to-next-to-leading order", *Comput. Phys. Commun.* **182** (2011) 2388, doi:10.1016/j.cpc.2011.06.008, arXiv:1011.3540.

[60] T. Melia, P. Nason, R. Rontsch, and G. Zanderighi, "W^+W^-, WZ and ZZ production in the POWHEG BOX", *JHEP* **11** (2011) 078, doi:10.1007/JHEP11(2011)078, arXiv:1107.5051.

[61] M. Czakon and A. Mitov, "Top++: A program for the calculation of the top-pair cross-section at hadron colliders", *Comput. Phys. Commun.* **185** (2014) 2930, doi:10.1016/j.cpc.2014.06.021, arXiv:1112.5675.

[62] S. Alioli, P. Nason, C. Oleari, and E. Re, "NLO single-top production matched with shower in POWHEG: *s*- and *t*-channel contributions", *JHEP* **09** (2009) 111, doi:10.1088/1126-6708/2009/09/111, arXiv:0907.4076.

[63] GEANT4 Collaboration, "GEANT4 — a simulation toolkit", *Nucl. Instr. Meth. A* **506** (2003) 250, doi:10.1016/S0168-9002(03)01368-8.

[64] T. Sjöstrand et al., "An Introduction to PYTHIA 8.2", *Comput. Phys. Commun.* **191** (2015) 159, doi:10.1016/j.cpc.2015.01.024, arXiv:1410.3012.

[65] W. Beenakker, R. Höpker, M. Spira, and P. M. Zerwas, "Squark and gluino production at hadron colliders", *Nucl. Phys. B* **492** (1997) 51, doi:10.1016/S0550-3213(97)80027-2, arXiv:hep-ph/9610490.

[66] A. Kulesza and L. Motyka, "Threshold Resummation for Squark-Antiquark and Gluino-Pair Production at the LHC", *Phys. Rev. Lett.* **102** (2009) 111802, doi:10.1103/PhysRevLett.102.111802, arXiv:0807.2405.

[67] A. Kulesza and L. Motyka, "Soft gluon resummation for the production of gluino-gluino and squark-antiquark pairs at the LHC", *Phys. Rev. D* **80** (2009) 095004, doi:10.1103/PhysRevD.80.095004, arXiv:0905.4749.

[68] W. Beenakker et al., "Soft-gluon resummation for squark and gluino hadroproduction", *JHEP* **09** (2009) 041, doi:10.1088/1126-6708/2009/12/041, arXiv:0909.4418.

[69] W. Beenakker et al., "Squark and gluino hadroproduction", *Int. J. Mod. Phys. A* **26** (2011) 2637, doi:10.1142/S0217751X11053560, arXiv:1105.1110.

[70] P. M. Nadolsky et al., "Implications of CTEQ global analysis for collider observables", *Phys. Rev. D* **78** (2008) 013004, doi:10.1103/PhysRevD.78.013004, arXiv:0802.0007.

[71] A. D. Martin, W. J. Stirling, R. S. Thorne, and G. Watt, "Parton distributions for the LHC", *Eur. Phys. J. C* **63** (2009) 189, `doi:10.1140/epjc/s10052-009-1072-5`, `arXiv:0901.0002`.

[72] CMS Collaboration, "The fast simulation of the CMS detector at LHC", *J. Phys. Conf. Ser.* **331** (2011) 032049, `doi:10.1088/1742-6596/331/3/032049`.

[73] NNPDF Collaboration, "Parton distributions for the LHC Run II", *JHEP* **04** (2015) 040, `doi:10.1007/JHEP04(2015)040`, `arXiv:1410.8849`.

[74] CMS Collaboration, "Event generator tunes obtained from underlying event and multiparton scattering measurements", *Eur. Phys. J. C* **76** (2016) 155, `doi:10.1140/epjc/s10052-016-3988-x`, `arXiv:1512.00815`.

[75] CMS Collaboration, "Particle-flow event reconstruction in CMS and performance for jets, taus, and $E\!\!\!/_T$", CMS Physics Analysis Summary CMS-PAS-PFT-09-001, 2009.

[76] CMS Collaboration, "Commissioning of the particle-flow event with the first LHC collisions recorded in the CMS detector", CMS Physics Analysis Summary CMS-PAS-PFT-10-001, 2010.

[77] CMS Collaboration, "Performance of photon reconstruction and identification with the CMS detector in proton-proton collisions at $\sqrt{s} = 8$ TeV", *JINST* **10** (2015) P08010, `doi:10.1088/1748-0221/10/08/P08010`, `arXiv:1502.02702`.

[78] CMS Collaboration, "Performance of electron reconstruction and selection with the CMS detector in proton-proton collisions at $\sqrt{s} = 8$ TeV", *JINST* **10** (2015) P06005, `doi:10.1088/1748-0221/10/06/P06005`, `arXiv:1502.02701`.

[79] CMS Collaboration, "Performance of CMS muon reconstruction in pp collision events at $\sqrt{s} = 7$ TeV", *JINST* **7** (2012) P10002, `doi:10.1088/1748-0221/7/10/P10002`, `arXiv:1206.4071`.

[80] M. Cacciari, G. P. Salam, and G. Soyez, "The anti-k_t jet clustering algorithm", *JHEP* **04** (2008) 063, `doi:10.1088/1126-6708/2008/04/063`, `arXiv:0802.1189`.

[81] M. Cacciari and G. P. Salam, "Pileup subtraction using jet areas", *Phys. Lett. B* **659** (2008) 119, `doi:10.1016/j.physletb.2007.09.077`, `arXiv:0707.1378`.

[82] CMS Collaboration, "Determination of jet energy calibration and transverse momentum resolution in CMS", *JINST* **6** (2011) P11002, `doi:10.1088/1748-0221/6/11/P11002`, `arXiv:1107.4277`.

[83] CMS Collaboration, "Identification of b-quark jets with the CMS experiment", *JINST* **8** (2013) P04013, `doi:10.1088/1748-0221/8/04/P04013`, `arXiv:1211.4462`.

[84] CMS Collaboration, "Identification of b quark jets at the CMS Experiment in the LHC Run 2", CMS Physics Analysis Summary CMS-PAS-BTV-15-001, 2016.

[85] CMS Collaboration, "Missing transverse energy performance of the CMS detector", *JINST* **6** (2011) P09001, `doi:10.1088/1748-0221/6/09/P09001`, `arXiv:1106.5048`.

[86] CMS Collaboration, "Identification and filtering of uncharacteristic noise in the CMS hadron calorimeter", *JINST* **5** (2010) T03014, `doi:10.1088/1748-0221/5/03/T03014`, `arXiv:0911.4881`.

[87] Z. Bern et al., "Driving Missing Data at Next-to-Leading Order", *Phys. Rev. D* **84** (2011) 114002, `doi:10.1103/PhysRevD.84.114002`, `arXiv:1106.1423`.

[88] ATLAS Collaboration, "Measurement of the Inelastic Proton-Proton Cross Section at $\sqrt{s} = 13$ TeV with the ATLAS Detector at the LHC", `arXiv:1606.02625`. Submitted to *Phys. Rev. Lett.*

[89] CMS Collaboration, "Measurement of the differential cross section for top quark pair production in pp collisions at $\sqrt{s} = 8$ TeV", *Eur. Phys. J. C* **75** (2015) 542, `doi:10.1140/epjc/s10052-015-3709-x`, `arXiv:1505.04480`.

[90] J. S. Conway, "Incorporating Nuisance Parameters in Likelihoods for Multisource Spectra", in *PHYSTAT 2011 Workshop on Statistical Issues Related to Discovery Claims in Search Experiments and Unfolding*, H. B. Prosper and L. Lyons, eds., p. 115. CERN, 2011. `doi:10.5170/CERN-2011-006`.

[91] J. K. Lindsey, "Parametric Statistical Inference". Oxford University Press, 1996. ISBN 0-19-852359-9.

[92] J. Alwall, P. Schuster, and N. Toro, "Simplified Models for a First Characterization of New Physics at the LHC", *Phys. Rev. D* **79** (2009) 075020, `doi:10.1103/PhysRevD.79.075020`, `arXiv:0810.3921`.

[93] J. Alwall, M.-P. Le, M. Lisanti, and J. G. Wacker, "Model-independent jets plus missing energy searches", *Phys. Rev. D* **79** (2009) 015005, `doi:10.1103/PhysRevD.79.015005`, `arXiv:0809.3264`.

[94] D. Alves et al., "Simplified models for LHC new physics searches", *J. Phys. G* **39** (2012) 105005, `doi:10.1088/0954-3899/39/10/105005`, `arXiv:1105.2838`.

[95] G. Cowan, K. Cranmer, E. Gross, and O. Vitells, "Asymptotic formulae for likelihood-based tests of new physics", *Eur. Phys. J. C* **71** (2011) 1554, `doi:10.1140/epjc/s10052-011-1554-0,10.1140/epjc/s10052-013-2501-z`, `arXiv:1007.1727`. [Erratum: *Eur. Phys. J. C* **73** (2013) 2501].

[96] ATLAS and CMS Collaborations, and LHC Higgs Combination Group, "Procedure for the LHC Higgs boson search combination in Summer 2011", Technical Report CMS-NOTE-2011-005 ATL-PHYS-PUB-2011-11, CERN, Geneva, 2011.

[97] T. Junk, "Confidence level computation for combining searches with small statistics", *Nucl. Instr. Meth. A* **434** (1999) 435, `doi:10.1016/S0168-9002(99)00498-2`, `arXiv:9902006`.

[98] A. L. Read, "Presentation of search results: the CL_s technique", *J. Phys. G* **28** (2002) 2693, `doi:10.1088/0954-3899/28/10/313`.

[99] CMS Collaboration, "CMS Luminosity Measurement for the 2015 Data Taking Period", CMS Physics Analysis Summary CMS-PAS-LUM-15-001, 2016.

[100] CMS Collaboration, "Search for top-squark pair production in the single-lepton final state in pp collisions at $\sqrt{s} = 8$ TeV", *Eur. Phys. J. C* **73** (2013) 2677, `doi:10.1140/epjc/s10052-013-2677-2`, `arXiv:1308.1586`.